SUPPORTING INFORMATION

for

In Situ Allocation of a Monomer in Pectin-*g*-Terpolymer Hydrogels and Effect of Comonomer Compositions on Superadsorption of Metal Ions/Dyes

Nayan Ranjan Singha,[*,†] *Manas Mahapatra,*[†] *Mrinmoy Karmakar,*[†] *Himarati Mondal,*[†] *Arnab Dutta,*[†] *Mousumi Deb,*[†] *Madhushree Mitra,*[$] *Chandan Roy,*[†] *Pijush Kanti Chattopadhyay,*[$] *and Dilip K. Maiti*[*,‡]

[†]*Advanced Polymer Laboratory, Department of Polymer Science and Technology, and* [§]*Department of Leather Technology, Government College of Engineering and Leather Technology (Post-Graduate), Maulana Abul Kalam Azad University of Technology, Salt Lake, Kolkata 700106, West Bengal, India*

[‡]*Department of Chemistry, University of Calcutta, 92, A. P. C. Road, Kolkata 700009, India*

Corresponding Authors

[*]E-mail: drs.nrs@gmail.com (N.R.S.).

[*]E-mail: maitidk@yahoo.com (D.K.M.).

ORCID

Nayan Ranjan Singha: 0000-0002-0219-1790

EXPERIMENTAL SECTION

Characterization. PANIPNs were characterized by Fourier transform infrared (FTIR) spectroscopy through Spectrum-2, Singapore in the range from 4000 to 400 cm^{-1}; ^{1}H-/^{13}C-nuclear magnetic resonance (^{1}H-/^{13}C-NMR) spectroscopy using Bruker-Advance Digital 300 MHz in $CDCl_3$ solvent with TMS as an internal reference/JEOL ECX400, at the proton frequency of 400 MHz; X-ray photoelectronic spectroscopy (XPS) via ESCA+, Omicron nanotechnology, Oxford Instrument Germany, equipped with Al Source (k_α radiation hν = 1486.7 ev) monochromator, operating at 15 kv, and 20 mA; thermogravimetric analysis (TGA) using Pyris6 TGA, The Netherlands in N_2 atmosphere with flow, and scanning rates of 20.0 cm^3 min^{-1} and 10 °C min^{-1}, respectively, from 30 to 700 °C; differential scanning calorimetry (DSC) via Pyris6 DSC, the Netherlands in N_2 atmosphere with the flow rate of 20.0 cm^3 min^{-1}, within 30–442 °C; X-ray diffraction (XRD) by X'Pert PRO, PANalytical B.V., the Netherlands, using Ni-filtered CuK_α radiation (λ = 1.5406 Å) having angle of diffraction, within 5–100°; scanning electron microscope (SEM), and energy dispersive X-ray (EDX) using ZEISS EVO-MA 10 having resolution of 3 nm with W filament and Sb as sources, and rheological analyses through Anton Paar MCR 102 rheometer. PANIPNs were also characterized by measuring network parameters, such as crosslink densities (i.e., CDs, ρ_c), and average molecular weights between crosslinks (i.e., M_c), LCST, % gel content (i.e., % GC) content, amount of % –COOH, pH at point of zero charge (i.e., pH_{PZC}), and equilibrium swelling ratios (i.e., ESRs) at different pH_i and temperature. RSM based optimization was performed by Design Expert 7.0.0. All graphics based analyses were carried out using Origin 9.0 software.

Methodology. SF and M(II/III) solutions of varying concentrations (i.e., 10–200 and 10–60 ppm for dye and M(II/III), respectively) were prepared by exact dilution of 1000 ppm stock solutions. In the present study, 0.025 g of dry PANIPNs was added to 50 mL buffered solutions of adsorbates with constant stirring at 300 rpm. The progress of adsorption was monitored by withdrawing supernatant solution after definite time intervals and measuring absorbance at λ_{max} using UV-vis spectrophotometer (PerkinElmer Lambda 365) and atomic absorption spectrometer (PerkinElmer A-ANALYST 100) for dyes and M(II/III), respectively. From the pre-calibrated equations, adsorbate concentrations (i.e., C_t) were calculated, from which q_t (mg g^{-1}) values were determined using Equation S1.

$$q_t = \frac{(C_0 - C_t)V}{m_s} \quad \text{(S1)}$$

Here, C_0/C_t (ppm), V (mL), and m_s (g) are feed dye concentrations at $t = 0/t$, volume of dye solution and mass of PANIPNs, respectively. Equilibrium AC (i.e., q_e, mg g^{-1}) was obtained via replacing C_t by C_e in Equation S1.

Swelling and pH/temperature reversibility studies of PANIPNs. For swelling and deswelling studies, hydrogels were immersed for a time period of 1 hr at of pH_i = 2 and 12, respectively. For analyzing the temperature reversibility, hydrogels were allowed to swell and deswell at 323 and 293 K, respectively. Indeed, all the cycles were continued repetitively until the loss of hydrogel stability.

Calculation of % –COOH, pH_{PZC}, % GC, and network parameters of PANIPNs. The amount of –COOH was estimated by a method reported elsewhere using Equation S2.[S1]

$$\%-\mathrm{COOH} = [(C_{\mathrm{NaOH}} \times V_{\mathrm{NaOH}}) - (C_{\mathrm{HCl}} \times V_{\mathrm{HCl}}) \times 45 \times 10^{-3} \times 100] / 0.05 \quad \text{(S2)}$$

The pH_{PZC} of both the PANIPNs was estimated by taking 0.05 g of xerogel in 50 mL buffer solutions of different initial pH (i.e., pH_i = 2 to 10). After 72 hrs of immersion, final pH (i.e., pH_f) of all the solutions were estimated. The difference of these pH_f and pH_i was plotted wioth pH_i to find the pH_{PZC}.

The % GC of the PANIPNs were estimated by the method reported elsewhere,[S1] using Equation S3.

$$\%\,GC = \frac{W_d}{W_i} \times 100 \tag{S3}$$

The M_c of PANIPNs was calculated, using Equation S4, based on the network theory of Flory and Rehner.

$$M_c = -\frac{V_S \rho_p (\varphi_p^{1/3} - \frac{\varphi_p}{2})}{\ln(1-\varphi_p) + \varphi_p + \chi \varphi_p^2} \tag{S4}$$

Here, V_S, ρ_p, φ_p, and χ are molar volume of water, density of PANIPNs, volume fraction of swollen PANIPNs after attending the equilibrium, and interaction parameter of PANIPNs-water, respectively. However, V_S was calculated from density and molecular weight of PANIPNs. Equation S5 was employed to calculate φ_p from the known value of swelling ratio (i.e., m_w, g g^{-1}).

$$\varphi_p = \frac{1/\rho_p}{(m_w/0.99) + (1/\rho_p)} \tag{S5}$$

Indeed, χ was calculated from the Flory-Huggins theory, using Equation S6, in which a_w is the activity of water.

$$\ln a_w = \ln(1-\varphi_p) + \varphi_p + \chi \varphi_p^2 \tag{S6}$$

For pure component system (i.e., a_w = 1), Equation S6 can be rearranged to Equation S7.

$$\text{or, } \chi = \frac{\varphi_p}{3} + 0.5 \tag{S7}$$

Finally, crosslink density (i.e., ρ_c), in the PANIPNs network, was calculated using Equation S8.

$$\rho_c = \frac{M_0}{M_c} \tag{S8}$$

Here, molar mass of repeating unit per crosslink (i.e., M_0) is defined by Equation S9.

$$M_0 = \frac{n_{PN} M_{PN} + n_{CPOL} M_{CPOL}}{n_{PN} + n_{CPOL}} \tag{S9}$$

Here, n and M (n_{PN}, n_{CPOL}, $M_{PN,}$ and M_{CPOL}) represent moles of repeating units, and molar masses of PN and copolymer (i.e., CPOL) in PANIPNs, respectively. In fact, M_{CPOL} was taken as the average of respective contributions of the monomers in copolymer. Ignoring the marginal contribution of MBA and assuming only the presence of binary copolymerization, for incorporating PN in the matrix of CPOL by free radical solution polymerization reaction, the approximate copolymer composition of monomers was calculated using Equation S10.

$$\frac{M_{AA}}{M_{NIPAm}} = \frac{r_{AA} m_{AA}^2 + m_{AA} m_{NIPAm}}{r_{NIPAm} m_{NIPAm}^2 + m_{AA} m_{NIPAm}} \tag{S10}$$

Here, r_{AA}/r_{NIPAm} and m_{AA}/m_{NIPAm} are reactivity ratios and moles of AA/NIPAm, respectively. However, PANIPNs network was also characterized by measuring network parameters, such as M_c and ρ_c, based on the network theory of Flory and Rehner.

Adsorption isotherm studies of dye/M(II/III) onto PANIPN41 and PANIPN21. ACs (i.e., q_{max}, mg g^{-1}) of PANIPNs were estimated from the correlation of equilibrium AC (i.e., q_e, mg g^{-1}) and the residual adsorbate concentration at equilibrium (i.e., C_e). However, in the present study, adsorption isotherm studies of PANIPNs for M(II/III), such as Hg(II), Cd(II), Cr(III), and SF, were conducted by taking 50 mL of solutions within 5–100 and 5–30 ppm at constant pH_i = 7 and 9 for M(II/III) and SF, respectively, along with 0.025 g of PANIPNs at constant temperature (i.e., 293, 303, 313, and 323K) and 500 rpm. At definite time intervals, the supernatant solution

was withdrawn and the residual adsorbate concentration (i.e., C_t, ppm) was determined by UV-vis spectrophotometer and atomic absorption spectrometer for dye and M(II/III), respectively, via measuring absorbance (i.e., A_t) at λ_{max}. In fact, the adsorption data were analyzed using different isotherm models, such as Langmuir, Freundlich, and Temkin (Equations S11–S13) for the estimation of various model parameters to enlighten various aspects of adsorption mechanism.

$$q_e = q_{max} \frac{k_L C_e}{1 + k_L C_e} \tag{S11}$$

$$q_e = k_F C_e^{1/n} \tag{S12}$$

$$q_e = \frac{RT}{b_T} \ln(k_T C_e) \tag{S13}$$

Here, k_L, k_F, and k_T are the corresponding isotherm constants and q_{max}, n, b_T, and k_T are the corresponding parameters of the isotherm models. R_L can be defined by the Equation S14.

$$R_L = \frac{1}{1 + k_L C_0} \tag{S14}$$

Kinetics of adsorption. Adsorption kinetics are carried out to identify the mechanism, rate determining step, and diffusion characteristics of the isothermal adsorption process. In the present study, kinetics studies were executed by taking 0.025 g of both PANIPNs at different initial concentrations of SF/M(II/III), constant pH_i, and various temperatures. The kinetic data were analyzed via non-linear pseudofirst/second order kinetics models (Equations S15/S16).

$$q_t = q_e[1 - \exp(-k_1 t)] \tag{S15}$$

$$q_t = q_e\left(1 - \frac{1}{1 + k_2 q_e t}\right) \tag{S16}$$

Here, k_1 (min^{-1})/k_2 (g mg^{-1} min^{-1}) represent pseudofirst/second order rate constants.

Thermodynamics of adsorption. The thermodynamic parameters, such as changes in enthalpy (i.e., ΔH^0), entropy (i.e., ΔS^0) and Gibbs free energy (i.e., ΔG^0) were measured to apprehend the effect of temperature on adsorption isotherm. The spontaneity of adsorption process is confirmed by the negative ΔG^0, as expressed by Equation S17.

$$\Delta G^0 = -RT \ln k_d \tag{S17}$$

Here, k_d, known as distribution coefficient, can be defined by the Equation S18.

$$k_d = \frac{q_e}{C_e} \tag{S18}$$

Here, ΔH^0 and ΔS^0 can be determined from the slope and intercept of the linearized form of van't Hoff's equation, respectively, as expressed in Equation S19.

$$\ln k_c = -\frac{\Delta H^0}{RT} + \frac{\Delta S^0}{R} \tag{S19}$$

Effect of temperature on adsorption kinetics. The effect of temperature on kinetics was established by taking 25 ppm M(II/III) solutions at $pH_i = 7$ and 0.025 g of PANIPN21/41 at 293, 303, 313, and 323 K. As all the M(II/III) followed pseudosecond order kinetics, k_2 at different temperatures could be interrelated by the following Arrhenius type equation.

$$\ln k_2 = \ln k_0 - \frac{E_a}{RT} \tag{S20}$$

Here, k_0 and E_a are temperature independent factor (g mg^{-1} min^{-1}) and activation energy of adsorption (kJ mol^{-1}), respectively. In fact, from the slope of the linearized $\ln k_2$ vs. $1/T$ plot, E_a can be evaluated.

RESULTS AND DISCUSSION

Experimental design and model development for the synthesis of PANIPN

Table S1. Resolution-IV Design for Screening of Important Process Variables in Phase-I

run no.	amount of SA (wt %)	total amount of PPS + SBS (wt %)	amount of PN (wt %)	amount of MBA (wt %)	pH_i (–)	temperature (K)	ESR (–)
1	66.67	1.00	0.10	0.10	4	303	129
2	95.24	1.00	0.10	0.10	12	303	203
3	66.67	4.00	0.10	0.10	12	323	210
4	95.24	4.00	0.10	0.10	4	323	155
5	66.67	1.00	0.50	0.10	12	323	184
6	95.24	1.00	0.50	0.10	4	323	155
7	66.67	4.00	0.50	0.10	4	303	156
8	95.24	4.00	0.50	0.10	12	303	214
9	66.67	1.00	0.10	0.40	4	323	130
10	95.24	1.00	0.10	0.40	12	323	204
11	66.67	4.00	0.10	0.40	12	303	206
12	95.24	4.00	0.10	0.40	4	303	176
13	66.67	1.00	0.50	0.40	12	303	170
14	95.24	1.00	0.50	0.40	4	303	140
15	66.67	4.00	0.50	0.40	4	323	157
16	95.24	4.00	0.50	0.40	12	323	231
17	80.955	2.50	0.30	0.25	8	313	184
18	80.955	2.50	0.30	0.25	8	313	184
19	80.955	2.50	0.30	0.25	8	313	184

SA: sodium acrylate, PPS: potassium persulfate, SBS: sodium bisulfite, PN: pectin, MBA: *N, N'*-methylenebisacrylamide, and ESR: percent equilibrium swelling ratio

Table S2. ANOVA for Phase-1

source	sum of squares	degrees of freedom	mean square	*F* value	*p*-value
model	15098.75	6	2516.46	108.23	< 0.0001*
amount of SA (A)	1156.00	1	1156.00	49.72	< 0.0001*
amount of PPS + SBS (B)	2256.25	1	2256.25	97.04	< 0.0001*
pH_i (E)	11236.00	1	11236.00	483.27	< 0.0001*
AB	110.25	1	110.25	4.74	0.0484*
AD	100.00	1	100.00	4.30	0.0585
CF	240.25	1	240.25	10.33	0.0068*
curvature	151.74	1	151.74	6.53	0.0240
residual	302.25	13	23.25		
lack of fit	302.25	11	27.48		
pure error	0.00	2	0.00		
cor. total	15552.74	20			
std. dev.	4.82	R^2	0.9804		
mean	177.47	adj. R^2	0.9713		
CV %	2.72	pred. R^2	0.9386		
PRESS	955.26	adeq. precision	34.0380		

*significant

Table S3. Central Composite Design (CCD) of Experiment

run no.	amount of SA (wt %)	total PPS + SBS (wt %)	pH_i (–)	ESR (–)
1	66.67	2.00	5.00	63
2	95.24	2.00	5.00	71
3	66.67	4.00	5.00	60
4	95.24	4.00	5.00	75
5	66.67	2.00	10.00	167
6	95.24	2.00	10.00	200
7	66.67	4.00	10.00	154
8	95.24	4.00	10.00	200
9	56.93	3.00	7.50	80
10	100.00	3.00	7.50	162
11	80.95	1.32	7.50	80
12	80.95	4.68	7.50	70
13	80.95	3.00	3.30	118
14	80.95	3.00	11.70	310
15	80.95	3.00	7.50	216
16	80.95	3.00	7.50	216
17	80.95	3.00	7.50	216
18	80.95	3.00	7.50	216
19	80.95	3.00	7.50	216
20	80.95	3.00	7.50	216

SA: sodium acrylate, PPS: potassium persulfate, SBS: sodium bisulfite, and ESR: percent equilibrium swelling ratio

Table S4. ANOVA Statistics of CCD

source	sum of squares	degrees of freedom	mean square	*F* value	*p*-value
model	1.01×10^5	9	11262.61	6013.61	< 0.0001*
amount of SA (A)	1999.85	1	1999.85	1067.81	< 0.0001*
amount of PPS + SBS (B)	60.81	1	60.81	32.47	0.0002*
pH_i (E)	43968.88	1	43968.88	23476.94	< 0.0001*
AB	50.00	1	50.00	26.70	0.0004*
AE	392.00	1	392.00	209.31	< 0.0001*
BE	24.50	1	24.50	13.08	0.0047*
A^2	17907.58	1	17907.58	9561.65	< 0.0001*
B^2	36488.20	1	36488.20	19482.67	< 0.0001*
E^2	14.39	1	14.39	7.68	0.0197*
residual	18.73	10	1.87		
lack of fit	18.73	5	3.75		
pure error	0.00	5	0.00		
cor. total	1.01×10^5	19			
std. dev.	1.37		R^2	0.9998	
mean	155.30		adj. R^2	0.9996	
CV %	0.88		pred. R^2	0.9985	
PRESS	154.87		adeq. precision	258.2380	

*significant

Calculation of LCST, % –COOH, pH_{PZC}, % GC, and network parameters of PANIPNs

The grafting of PN within copolymer network of thermosensitive PANIPNs was envisaged by the variation of LCST. In order to determine the LCST of PANIPNs and respective copolymers, 0.01 g of hydrogels were allowed to swell in double distilled water for 24 h, followed by performing DSC in N_2 atmosphere within 5–100 ^oC at scanning rate of 5 ^oC min^{-1}. In fact, the LCST of PANIPN41 and PANIPN21, appeared at 75.56 ^oC and 68.75 ^oC, were found to be slightly higher than copolymers(Figure S2g), emphasizing the relative enhancement of hydrophilic groups in PANIPNs. Thus, the increase in water swelling-deswelling reversibility of the PANIPNs, beyond the LCST of PNIPAm hydrogel, could be attributed to the presence of highly hydrophilic SA and PN moieties in the hydrogel network. The % –COOH content was found to be 9.84 and 4.95 % for PANIPN41 and PANIPN21,

Table S5. Variation of Physical Properties of PANIPNs

polymer (SA:NIPAm/MBA/ PPS+SBS/PN)	density (g mL^{-1})	swelling ratio in water (g/g)	volume fraction of swollen hydrogel (φ_p)	polymer-water interaction parameter (χ)	average molar mass between crosslink (Mc)	crosslink density (ρ_c)
PANIPN1 (**1:1**/0.20/2.00/0.50)	1.364	254.43	0.0028	0.50095	2.12×10^{11}	4.55×10^{-10}
PANIPN2 (**2:1**/0.20/2.00/0.50)	1.375	345.64	0.0021	0.50069	6.77×10^{11}	1.60×10^{-10}
PANIPN3 (**4:1**/0.20/2.00/0.50)	1.384	366.67	0.0020	0.50065	8.66×10^{11}	1.18×10^{-10}
PANIPN4 (**10:1**/0.20/2.00/0.50)	1.394	373.63	0.0019	0.50063	9.60×10^{11}	1.00×10^{-10}
PANIPN5 (4:1/**0.10**/2.00/0.50)	1.376	380.71	0.0018	0.50063	9.68×10^{11}	1.06×10^{-10}
PANIPN6 (4:1/**0.20**/2.00/0.50)	1.384	367.63	0.0019	0.50065	8.75×10^{11}	1.17×10^{-10}
PANIPN7 (4:1/**0.30**/2.00/0.50)	1.385	306.21	0.0023	0.50078	4.49×10^{11}	2.28×10^{-10}
PANIPN8 (4:1/**0.40**/2.00/0.50)	1.391	239.34	0.0030	0.50099	1.86×10^{11}	5.51×10^{-10}
PANIPN9 (4:1/0.20/**1.25**/0.50)	1.384	315.24	0.0023	0.50075	4.98×10^{11}	2.05×10^{-10}
PANIPN10 (4:1/0.20/**1.50**/0.50)	1.433	327.03	0.0021	0.50070	6.70×10^{11}	1.53×10^{-10}
PANIPN11 (4:1/0.20/**2.00**/0.50)	1.384	367.63	0.0019	0.50065	8.75×10^{11}	1.17×10^{-10}
PANIPN12 (4:1/0.20/**2.50**/0.50)	1.373	255.14	0.0028	0.50094	2.21×10^{11}	4.63×10^{-10}
PANIPN13 (4:1/0.20/2.00/**0.25**)	1.355	327.21	0.0022	0.50074	5.17×10^{11}	1.98×10^{-10}
PANIPN14 (4:1/0.20/2.00/**0.50**)	1.384	365.63	0.0020	0.50065	8.57×10^{11}	1.19×10^{-10}
PANIPN15 (4:1/0.20/2.00/**0.75**)	1.386	378.21	0.0019	0.50063	9.77×10^{11}	1.05×10^{-10}

SA: sodium acrylate, NIPAm: *N*-isopropylacrylamide, PPS: potassium persulfate, SBS: sodium bisulfite, and PN: Pectin

respectively, resulted by the relative variation of SA in PANIPNs. However, for the used PANIPNs, pH_{PZC} was found to be 7.07 and 6.66 for PANIPN41 and PANIPN21, respectively (Figure S2h). Again, % GC of PANIPNs was found to decrease from 71.47 % of PANIPN41 to 62.49 % in PANIPN21. The network parameters, such as average molecular weight between crosslink (i.e., M_c) and crosslink density (i.e., ρ_c), were obtained from swelling data of the hydrogels using Equations S4 and S8, respectively. The decrease in M_c with an enhancement of ρ_c was observed with progressive increase in the wt % of crosslinker, ascribed to the formation of greater number of networks. Similar results were also reflected by the increase in initiator amount from 1.25 to 2.0 wt % (Table S5). Indeed, the successive increase in wt % of PN in PANIPNs from 0.25 to 0.75 wt % resulted a decrease in ρ_c, attributed to the increase in viscosity of solution leading to a decrease in the efficiency of radical formation. A reverse trend of network parameters was also observed by the increase in SA:NIPAm ratio in the copolymer network from 1:1 to 10:1. In

this regard, the increment of NIPAm content, a large moiety compared to SA, resulted in better population of branched multiple side chains in the PANIPNs (Table S5).

FTIR analyses

Table S6. FTIR analyses of PN, TerP41, and PANIPN41

PN	TerP41	PANIPN41	assignment	ref.
–	–	3650 (w)	weak H-bonds	
–	3434 (b)	3435 (b)	mutual O–H/ N–H H-bonding	
–	–	2855 (w)	symmetric $–CH_2–$ *str*. of $–O–CH_2–$	
–	2352 (w)	2350 (w)	strong O–H/ O–H H-bonding	S2
–	1713 (sh)	–	H-bonded –COOH dimer	S3
–	1560 (s, b)	–	asymmetric COO^- *str*.	S3
–	–	1458 (w)	$–CH_2–$ *def*. of $–O–CH_2–$	
1444	–	–	$–OCH_2–$ *def*. of methyl ester of PN ring	
–	1411 (m)	–	symmetric COO^- *str*.	
–	1386 (m) /1365 (w)	1385 (m, s) /1365 (w)	doublet peaks of isopropyl groups of NIPAm	S4
–	1280	–	amide-III/C–N *str*.	S5
1265	–	–	C–O–C of ester	
1148	–	–	C–O–C *str*. peak of α-1,4- glycosidic link/ring	S6, S7
–	–	1169 (sh)	C–O–C *str*. peak of β-1,4-glycosidic link/ring	S7
1112	–	1112 (w)	C–O, C–C, C–C–H and O–C–H of PN ring	
1080	–	–	C–O *str*. and O–C–H *bending*	
1051	–	–	C–O/C–C of PN ring	
1030	–	–	O–C/C–C/C–C–H of PN ring	
1018	–	–	C–2C–3/C–2O–2/C–1O–1 of PN ring	
985/970	–	–	$–OCH_3$ of ester of PN ring	
–	–	874 (w)	β-D-glucose	
825–860	–	–	equatorial anomeric hydrogen	
–	787 (w)	–	H-bonded –COOH dimer	S5
–	661(m, s)	669	N–C=O in-plane *bending*	S5
–	–	473 (m), 460 (w), 453 (w)	C–O–C and branching	S8

w = weak, s = sharp, b = broad, sh = shoulder, and m = medium

Table S7. FTIR analyses of PANIPN41 and Hg(II)-/Cd(II)-/Cr(III)-/SF-PANIPN41

PANIPN41	Hg(II)-PANIPN41	Cd(II)-PANIPN41	Cr(III)-PANIPN41	SF	SF-PANIPN41/21	assignment	ref.
3435 (b)	3585 (s), 3526 (s)	3426 (b)	3435 (b)	3434 (b)	3435 (b)/ 3434 (b)	modification of mutual O–H/N–H H-bonds in Hg(II)-PANIPN41	S9
–	–	–	–	3119 (w)	–	aromatic C–H *str*. of SF	S10
2975	2973	2973	2975	–	2957/2956	change in $–CH_2–$ asymmetric *str*. due to C=O…H–C H-bonds	S11, S12
2925	2928	2935	2929	2926	2925/2925	C–H *str*. peak of $–CH_3$	
2855	2856	2855	2856	2854	2855/2854	symmetric $–CH_2–$ *str*. of $–O–CH_2–$	S13
2350 (w)	2352 (w)	–	–	2346 (w)	–/2379 (w), 2359 (w), 2351(w), 2345 (w), 2341 (w)	strong O–H/O–H H-bonding	S14
1734	1716	1720	1730	–	1721/1718	C=O *str*. of chelates	S15
1638	1614	1635	1632	–	1632/1634	asymmetric $–COO^–$ *str*. and C=O *str*. of secondary amide	
–	–	–	–	1611 (s)	–	N=C *str*. of SF	S10
–	–	–	–	1530 (m)/1490 (m)	–	aromatic ring C=C *str*. of SF	S10
1458 (w)	1458 (w)	1458 (w)	1458 (w)	–	–	$–CH_2–$ *def*. of $–O–CH_2–$	
–	–	–	–	–	1401/–	symmetric $COO^–$ *str*.	
1385 (m, s)	1385 (m, s)	1385 (m, s)	1385 (m, b)	–	–	$–CH_3$ bending of isopropyl groups of NIPAm merged with C–O and C–C *str*. of Cr(III) in Cr(III)-PANIPN41	S16
1365 (w)	–	–	–	–	–	one of the doublet peaks of isopropyl groups of NIPAm	S4
–	–	–	–	–	1327/1327	C–N *str*.	S10
–	–	–	1262	–	–	O–C=O *bending*	
1169	1167	1170	1168	–	1166/1168	asymmetric C–O–C *str*.	S17, S18
–	–	–	807	–	–	Cr–O/C–O *str*.	
–	–	–	608	–	–	Cr–O bond	S19
–	–	–	519	–	–	Cr–N bond	
–	509	–	–	–	–	Hg–N covalent bond	

w = weak, s = sharp, b = broad, and m = medium

In Hg(II)-PANIPN41, Hg–N covalent bonds were produced via dehydrogenation of numerous N–H groups, as realized from the arrival of symbolic Hg–N peak at 509 cm^{-1} and the

disappearance of secondary amide peak at 1638 cm^{-1} (Figure S3a). The loss of N–H groups eventually affected mutual O–H/N–H H-bonding in Hg(II)-PANIPN41, realized from the conversion of broad peak within 3000–3500 cm^{-1} into sharp O–H *str.* peaks at 3585 and 3526 cm^{-1}. In fact, preferential covalent bond formation among Hg(II) and amide could be attributed to the soft nature of Hg(II) cation, which was also responsible for weaker binding of Hg(II) with O–H, as reflected in the prevalence of almost undisturbed O–H/ O–H H-bonding peak at 2352 cm^{-1} in Hg(II)-PANIPN41. In contrast, unaffected mutual O–H/ N–H H-bonding and secondary amide in Cd(II)-/Cr(III)-PANIPN41 was ascribed to weaker binding abilities of both Cd(II) and Cr(III) with N–H of amides (Figure S3a, Table S7), as both Cd(II) and Cr(III) ions are relatively harder than Hg(II). Accordingly, as compared to Hg(II), stronger coordinating tendencies of both Cd(II) and Cr(III) ions with O-donor ligands were apprehended from the C=O *str.* of the respective chelates (Table S7) and complete disruption of strong O–H/O–H H-bonding peaks in Cd(II)-/Cr(III)-PANIPN41, along with the appearance of characteristic Cr–O, Cr–N peaks in Cr(III)-PANIPN41. Altogether, adsorptive binding of M(II/III) in PANIPN41 resulted in significant lowering of asymmetric $–COO^-$ peaks, whereas both *str.* and *bending* peaks of $–CH_3$ in NIPAm were unaffected in the M(II/III)-PANIPN41 (Table S7).

Intimate coulombic attractions/H-bonding between SF and PANIPN41/21 resulted in complete disappearance of three SF specific peaks in SF-PANIPN41/21 (Table S7). Consequently, significant modification of both weaker H-bonds (C=O…H–C) and mutual O–H/ N–H H-bonding was realized from substantial lowering of asymmetric $–CH_2–$ *str.*, C–O–C *str.*, and C=O *str.* of secondary amide/ester, along with disappearance of one of the doublet peak at 1365 cm^{-1}, ascribed to restricted bending of $–CH_3$ of NIPAm side chains in SF-PANIPN41/21. In this context, as compared to SF-PANIPN21, relatively extensive modification of the H-bonding environment in

SF-PANIPN41 could be realized from complete disappearance of strong O–H/O–H H-bonding in SF-PANIPN41, while the related characteristic peaks at 2379, 2359, 2351, 2345, and 2341 cm^{-1} remained intact in SF-PANIPN21 (Figure S3b and Table S7), with notable existence of C–N *str.* peak at 1327 cm^{-1} in PANIPN41/21. Notably, PANIPN41, bearing relatively higher proportion of $–COO^-$, was involved in stronger ionic interaction with SF cations, leading to possible replacement of H-bonds by coulombic attractions in SF-PANIPN41, resulting in higher AC of PANIPN41 than PANIPN21.

Table S8. Adsorption Thermodynamics Parameters of SF at Higher Concentration

concentration (ppm) /temperature (K)	$-\Delta G^0$ (kJ mol^{-1}) of SF/ for PANIPN41(PANIPN21)	$-\Delta H^0$ (kJ mol^{-1}) of SF/ for PANIPN41(PANIPN21)	ΔS^0 (J mol^{-1} K^{-1}) of SF/ for PANIPN41(PANIPN21)
40/293	6.08(2.19)		
40/303	5.46(2.03)	28.66(20.93)	–76.41(–50.78)
40/313	4.77(1.74)		
40/323	3.33(1.37)		
50/293	5.14(1.78)		
50/303	4.71(1.46)	24.99(24.27)	–67.21(–65.38)
50/313	3.69(1.06)		
50/323	2.89(0.352)		
60/293	4.37(1.30)		
60/303	3.87(0.89)	25.74(24.02)	–72.48(–67.57)
60/313	2.84(0.38)		
60/323	2.05(0.69)		
80/293	3.46(0.45)		
80/303	2.52(–0.12)	24.19(24.01)	–71.39(–71.64)
80/313	1.73(–1.15)		
80/323	1.01(–3.35)		
100/293	2.44(–0.27)		
100/303	1.72(–1.23)	21.32(23.64)	–64.46(–73.12)
100/313	1.07(–3.24)		
100/323	0.46(–)		

Table S9. Comparative Table

types of adsorbate	name of dye/ metal ion	name of adsorbent	adsorption capacity (mg g^{-1}) /pH_i/C_0 (ppm)/ temperature (K)	ref.
M(II/III)	Hg(II)	chitosan derivative adsorbent	9.02/3.0/60/298	S20
		multifunctional mesoporous material	21.05/–/1000/–	S21
		PAM/ATP[a]	192.50/7.0/100–900/303	S22
		MWCNTs[b]	84.66/6.0/400/298	S23
		CNTs/Fe_3O_4[c]	65.52/6.5/50/298	S24
		Ti(IV) iodovanadate cation exchanger (TIV)	17.20/6.0/20/293–323	S25
		4-aminoantipyrine immobilized bentonite	52.90/4.0/1/298	S26
		mesoporous silica-coated magnetic particles	14.00/2.0/10–60/–	S27
		chemically treated sawdust (*Acacia arabica*)	20.62/6.0/3/–	S28
		Si-DTC[d]	80.24/6.0/200/298	S29
		dithiocarbamate-anchored polymer/organosmectite composites	71.10/7.0/50/293	S30
		graphene/c-MWCNT[b]	93.30/–/50/298	S31
		graphene-MWCNT[b]	75.80/–/50/298	S31
		RGO[e]-MnO_2	9.50/–/1/303	S32
		RGO[e]-Ag	9.53/–/1/303	S32
		EDA-modified mPMMA microbeads[f]	9.08/5.0/5–700/298	S33
		CSTU[g]	135.00/5.0/100/303	S34
		PANIPN41[h]	78.44/7.0/30/303	TS^
		PANIPN21[i]	96.78/7.0/30/303	TS^
	Cd(II)	Si-DTC[d]	43.47/7.0/100/298	S29
		dithiocarbamate-anchored polymer/organosmectite composites	82.20/7.0/50/293	S30
		CS-co-MMB-co-PAA[j]	135.51/4.5–5.5/300/–	S35
		AC-Fe_3O_4-NPs modified with DBABT[k]	185.22/6.0/5/–	S36
		graphene oxide–Al13	89.74/6.0/10/298	S37
		mesoporous MCM-41	210.96/7.0/250/298	S38
		BiOBr microsphere	11.70/7.0/29/298	S39
		garden grass	17.60/4.0/50/303	S40
		biomass of nonliving, dried brown marine algae *Sargassum natans*, *Fucus vesiculosus*, and *Ascophyllum nodosum*	100.00/3.5/100/–	S41
		ANMP derived from PCBs[l]	230.06/3.5/450/293	S42
		polyaniline grafted chitosan	12.87/6.0/20–40/303	S43
		dead T. viride	10.95/6.0/26/320	S44
		polyvinyl alcohol-chelating sponge	125.11/5.5/560/293	S45
		dithiocarbamated-sporopollenin	7.09/7.0/15/293	S46
		MGO[m]	91.29/6.0/200/298	S47
		RGO[e]-Fe(O)/Fe_3O_4	1.91/7.0/2–6/298	S48
		functionalized graphene (GNS^{C8P})	30.05/6.2/–/–	S49
		functionalized graphene (GNS^{PF6})	73.42/6.2/–/–	S49
		GO[n]	14.90/5.6/–/–	S50
		GO-TiO_2	72.80/5.6/–/–	S50
		GO[n]	167.50/6.0/–/333	S51

		novel magnetic nanocomposite hydrogel (m-CVP)	53.20/5.5/20/298	S52
		EDA-modified mPMMA microbeads[f]	5.89/5.0/5–700/298	S33
		CSTU[g]	120.00/5.0/100/303	S34
		p(AMPS-c-VI)[o]	83.30/–/50–1000/–	S53
		PEI grafted magnetic porous adsorbent[p]	105.20/7.0/50/293	S54
		PANIPN41[h]	103.36/7.0/30/303	TS^
		PANIPN21[i]	83.97/7.0/30/303	TS^
	Cr(III)	AC-Fe_3O_4-NPs was modified with DBABT[k]	188.70/6.0/25/–	S36
		AC[q]	60.00/6.0/25/–	S36
		AC-Fe_3O_4-NP[r]	123.50/6.0/25/–	S36
		garden grass	38.80/4.0/50/303	S40
		RGO[e]-Fe(O)/Fe_3O_4	31.10/7.0/2–6/298	S48
		FABN[s]	387.00/5.5/52/283–313	S55
		AA@VTES@Fe_3O_4[t]	0.24/6.0/170/303	S56
		poly(amidoamine) modified GO[n]	4.15/–/1/298	S57
		magnetic p(AMPS)[u]	76.87/–/500/298	S58
		PANIPN41[h]	99.41/7.0/30/303	TS^
		PANIPN21[i]	83.11/7.0/30/303	TS^
Dye	SF	Al-Mont-EnPILC[v]	76.13/10.0/100/295	S59
		hydrogels prepared with sodium polyacrylate and 6 wt% of CM	9.45/–/10/–	S60
		PDA@SBP[w]	54.00/10.0/100/293	S61
		native SBP[x]	17.90/10.0/100/293	S61
		Au-NP-AC[y]	50.25/7.0/18/–	S62
		AC[q]	1.32/5.0/25/298	S63
		MWCNT[z]	43.42/1.0/25/298	S63
		$Cd(OH)_2$-NW-AC[aa]	76.92/5.0/25/298	S63
		MIL-101(Cr)-SO_3H	70.80/6.2/50/–	S64
		AC[q]	19.01/6.0/10/–	S65
		ZnO-NR-AC[ab]	55.25/6.0/10/–	S65
		NiS-NP-AC[ac]	46.00–52.00/8.1/5/–	S66
		HDTMA[ad]-modified Spirulina sp.	54.05/2.0/300/–	S67
		SDS/RM[ae]	89.40/4.0/50/308	S68
		pinapple peels	21.70/6.0/60/302	S69
		NaOH-treated rice husk	37.97/8.0/10/303	S70
		CuO-NPs[af]	53.67/12.0/154/303	S71
		CO_2 neutralized activated red mud	9.77/8.3/37/302	S72
		Cu-NWs-AC[ag]	34.00/5.5/15/–	S73
		MDMLG[ah]	137.53/12.0/105/–	S74
		PANIPN41[h]	127.61/9.0/30/303	TS^
		PANIPN21[i]	117.60/9.0/30/303	TS^

[a]polyacrylamide/attapulgite, [b]multi-walled carbon nanotubes, [c]carbon nanotube/magnetite nanocomposites, [d]silica-supported dithiocarbamate adsorbent, [e]reduced graphene oxide, [f]ethylene diamine modified magnetic polymethylmethacrylate microbeads, [g]cross-linked magnetic chitosan-phenylthiourea, [h]pectin-g-(TerP41), [i]pectin-g-(TerP21), [j]a chitosan-based hydrogel graft-copolymerized with methylenebisacrylamide and poly(acrylic acid), [k]activated carbon magnetized with Fe_3O_4 nanoparticles modified with 2-((2, 4-Dichloro-benzylidene)-amino)-benzenethiol, [l]activated non-metallic powder derived from printed circuit boards, [m]magnetic graphene oxide, [n]graphene oxide, [o]poly(2-acrylamido-2-methyl-1-propansulfonic acid-co-vinylimidazole), [p]polyethylenimine grafted magnetic porous adsorbent, [q]activated carbon, [r]activated carbon was magnetized with Fe_3O_4 nanoparticles, [s]fluorinated activated boron nitride, [t]the surface of Fe_3O_4 nanoparticles via the bridging function of a silane coupling agent to produce a magnetically-separable nanoadsorbent, [u]2-acrylamido-2-methyl-1-propansulfonic acid, [v]Al-Mont-EnPILC,

[w]polydopamine coated sea buckthornbranch powder, [x]sea buckthornbranchpowder, [y]Au loaded on activated carbon, [z]multiwalled carbon nanotube, [aa]cadmium hydroxide nanowire loaded on activated carbon, [ab]ZnO nanorod-loaded activated carbon, [ac]nickel sulfide nanoparticle-loaded activated carbon, [ad]hexadecyltrimethylammonium bromide, [ae]sodium dodecyl sulphate/red mud, [af]copper oxide nanoparticles, [ag]copper nanowires loaded on activated carbon, [ah]MgO decked multi-layered graphene, and ^this study.

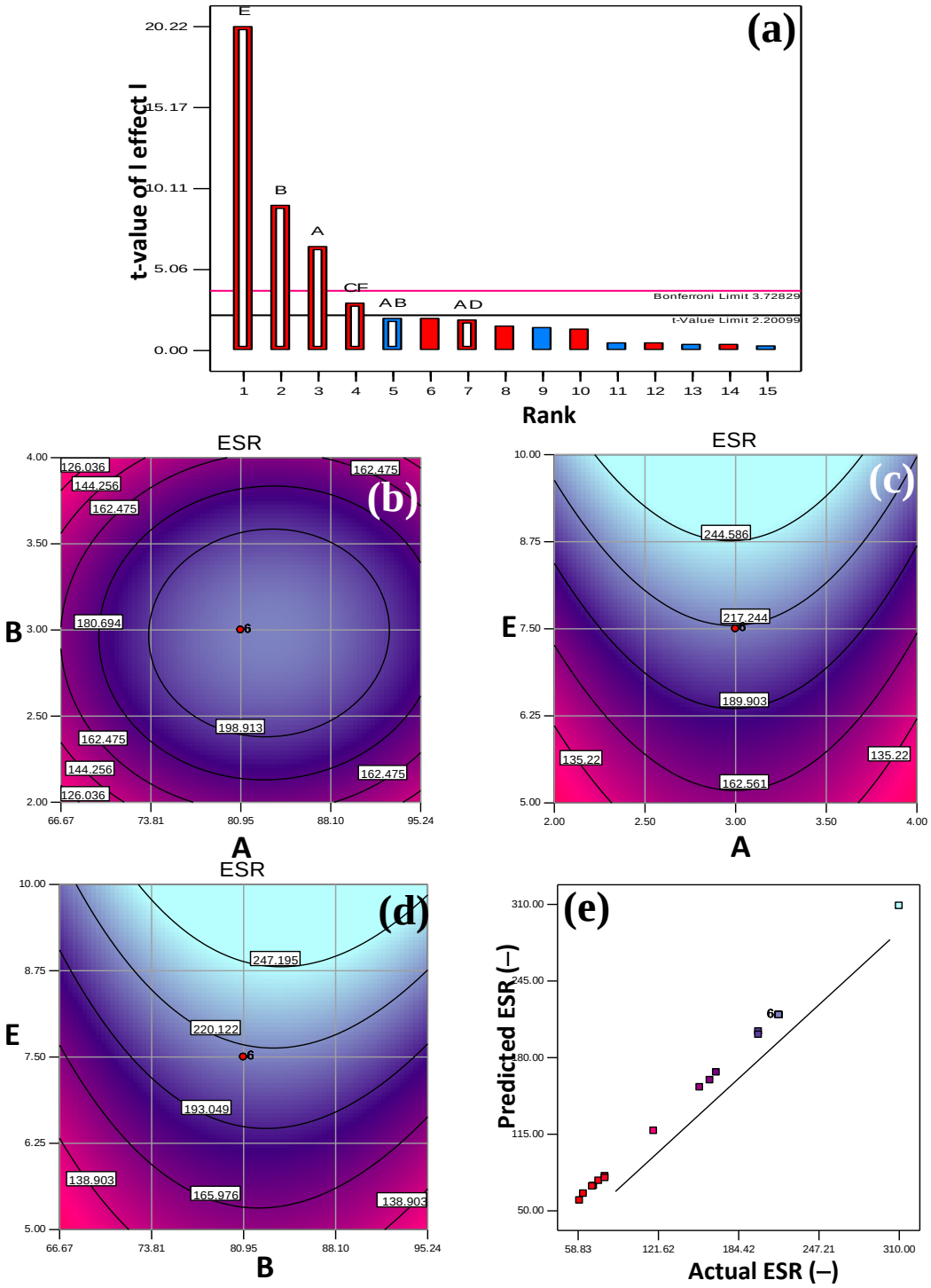

Figure S1. (a) Pareto chart, contour plots of ESR (–) vs. (b) initiator (B) and SA (A), (c) initiator (B) and pH (C), (d) SA and pH and (e) actual vs. predicted ESR

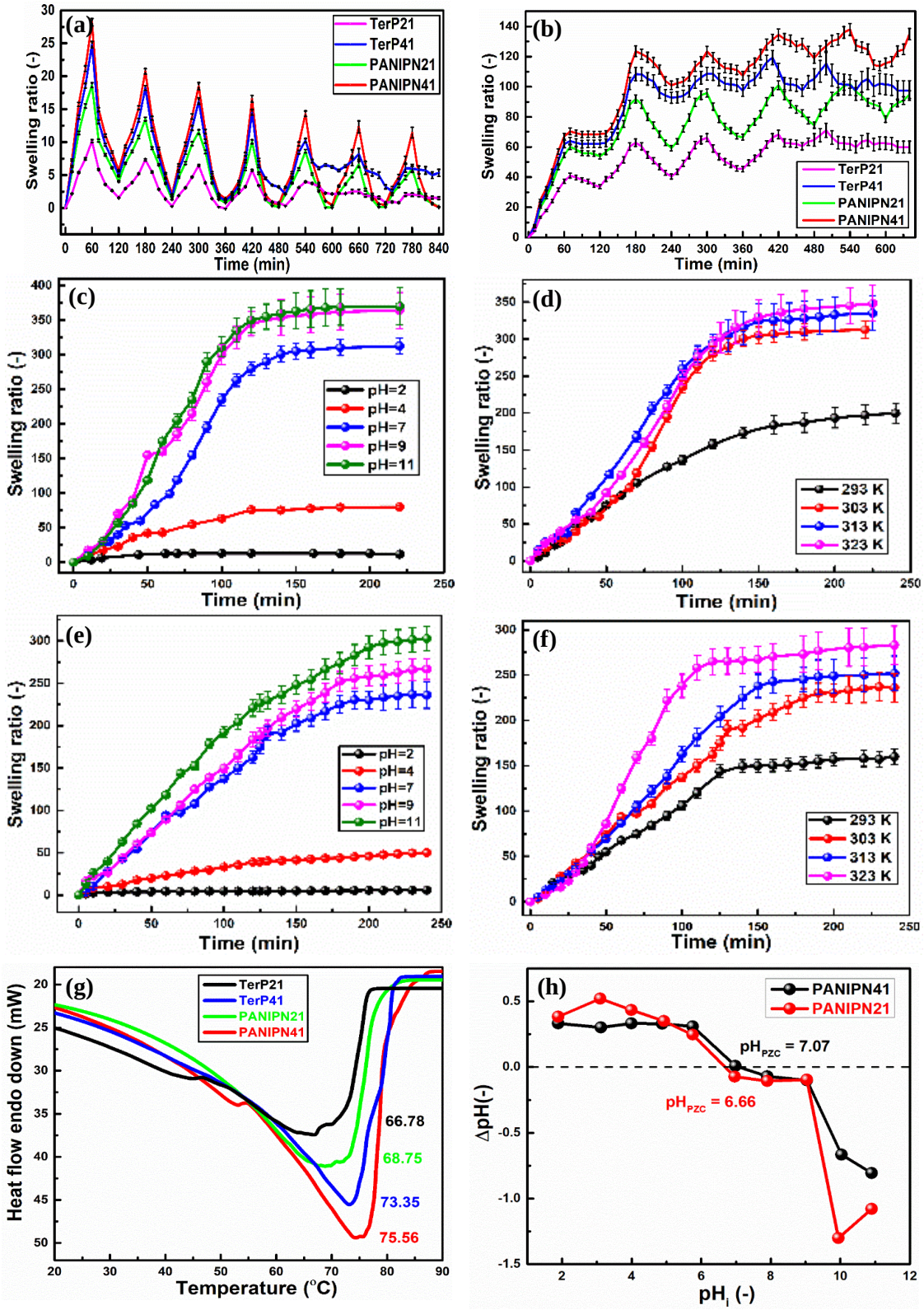

Figure S2. Swelling reversibility of TerP41, TerP21, PANIPN41 and PANIPN21 by variation of (a) pH_i (2/12), (b) temperature (293 K/323 K) and swelling of PANIPN41 and PANIPN21 at different (c, e) pH_i and (d, f) temperature; (g) LCST of TerP21, TerP41, PANIPN21 and PANIPN41; (h) pH_{PZC} of PANIPN21 and PANIPN41

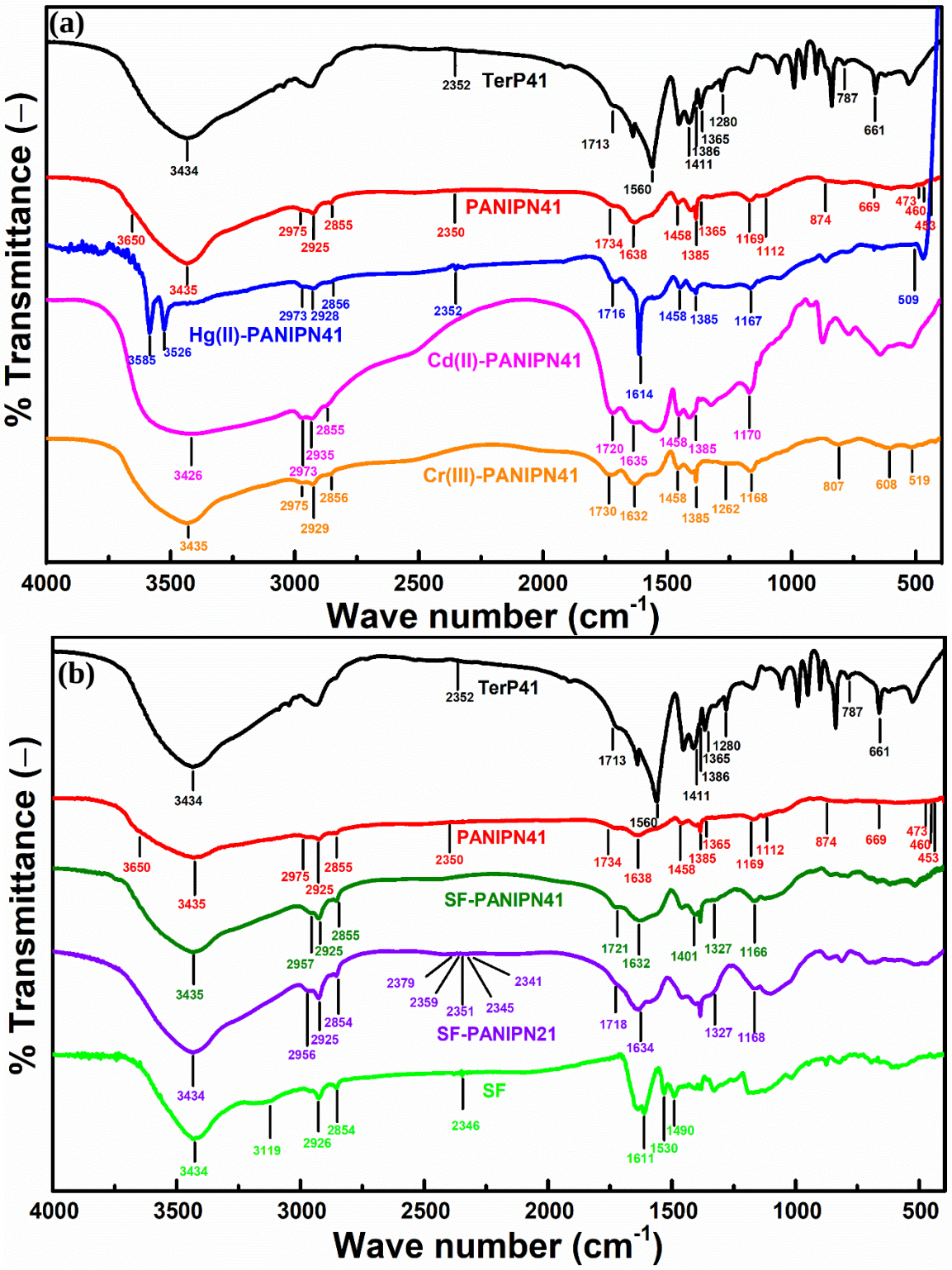

Figure S3. FTIR spectra of (a) TerP41, PANIPN41, Hg(II)-, Cd(II)- and Cr(III)-PANIPN41, and (b) TerP41, PANIPN41, SF-PANIPN41, SF-PANIPN21, and SF

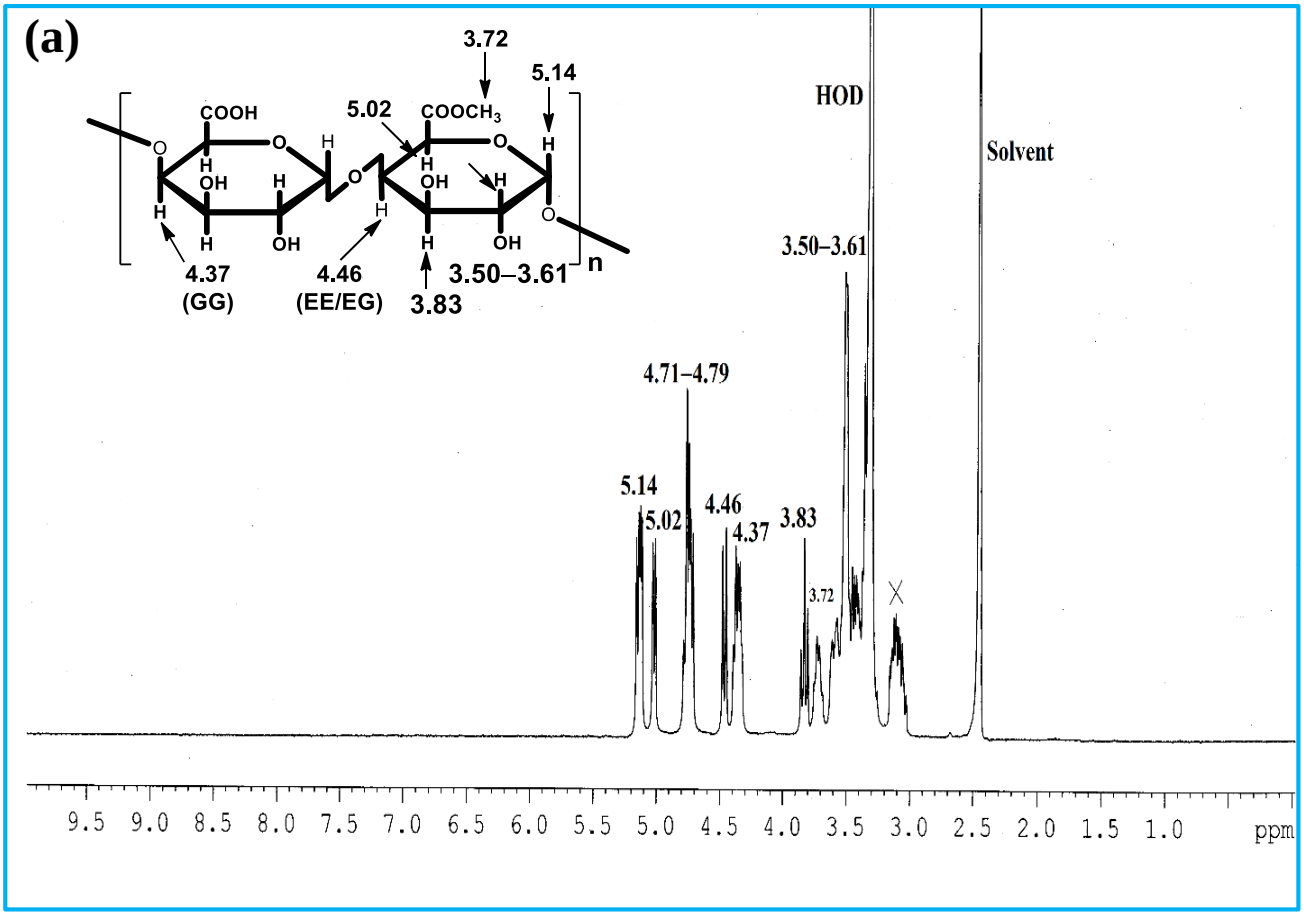
(a)
3.72
5.14
5.02
COOH
COOCH3
4.37
(GG)
4.46
(EE/EG)
3.83
3.50–3.61
n
HOD
Solvent
3.50–3.61
4.71–4.79
5.14
5.02
4.46
4.37
3.83
3.72
X
9.5 9.0 8.5 8.0 7.5 7.0 6.5 6.0 5.5 5.0 4.5 4.0 3.5 3.0 2.5 2.0 1.5 1.0
ppm

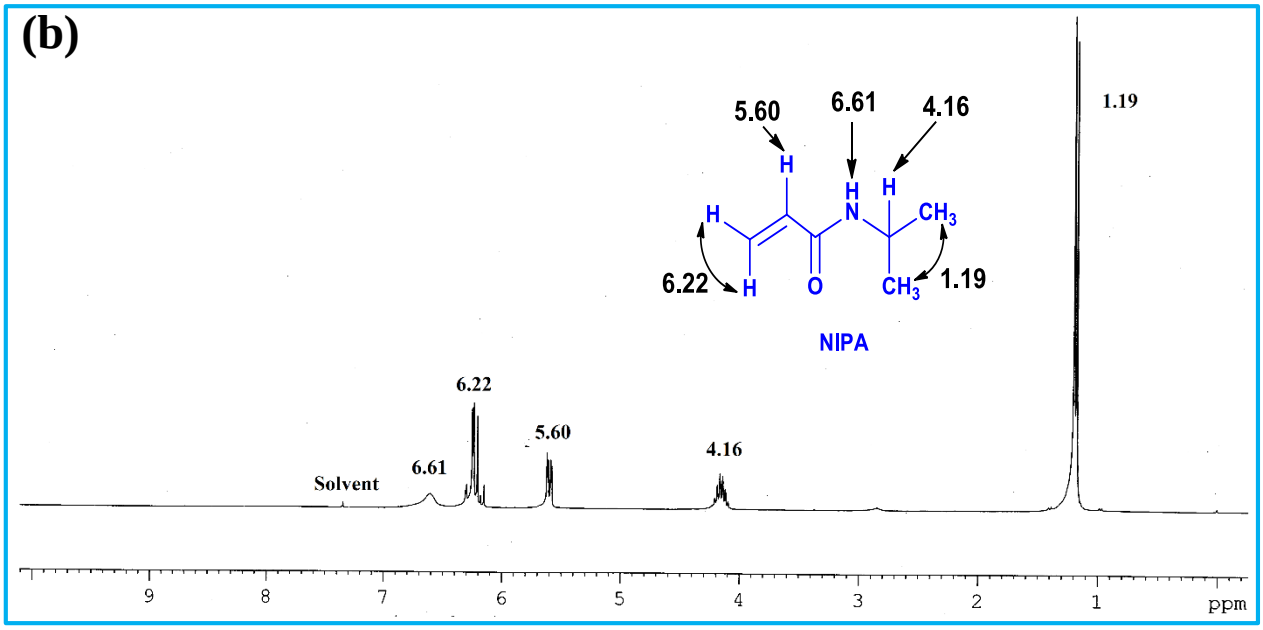
(b)
5.60
6.61
4.16
1.19
6.22
1.19
NIPA
6.22
5.60
4.16
6.61
Solvent
9
8
7
6
5
4
3
2
1
ppm

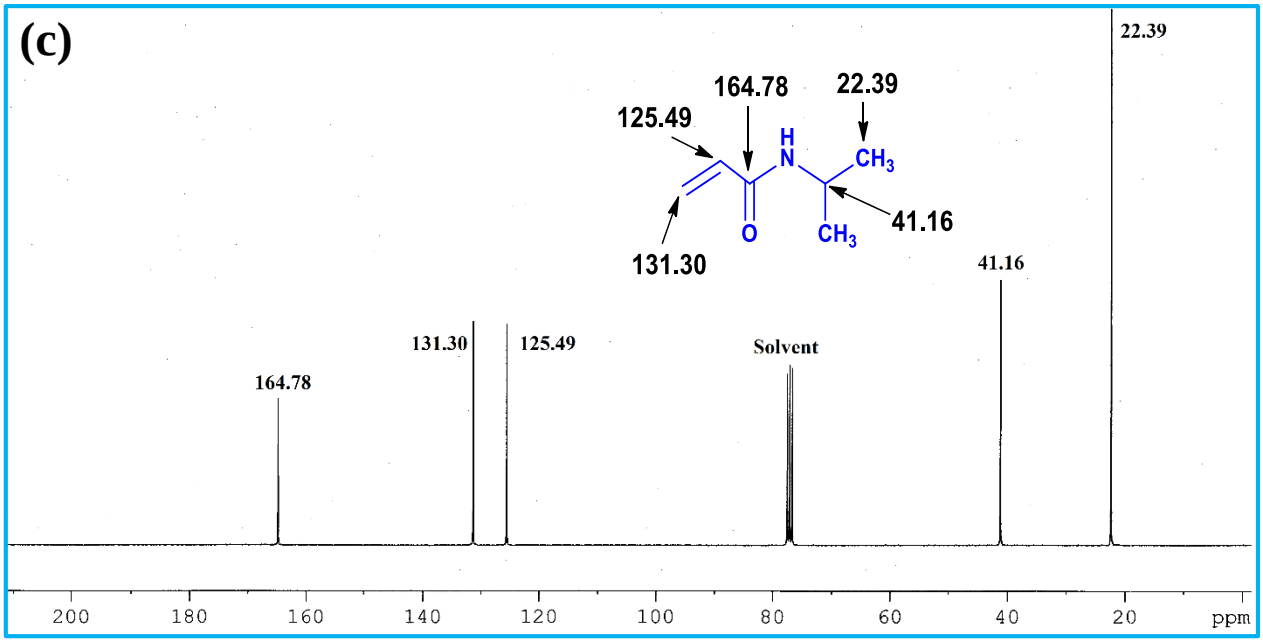
(c)
22.39
164.78
22.39
125.49
41.16
131.30
41.16
131.30
125.49
Solvent
164.78
200
180
160
140
120
100
80
60
40
20
ppm

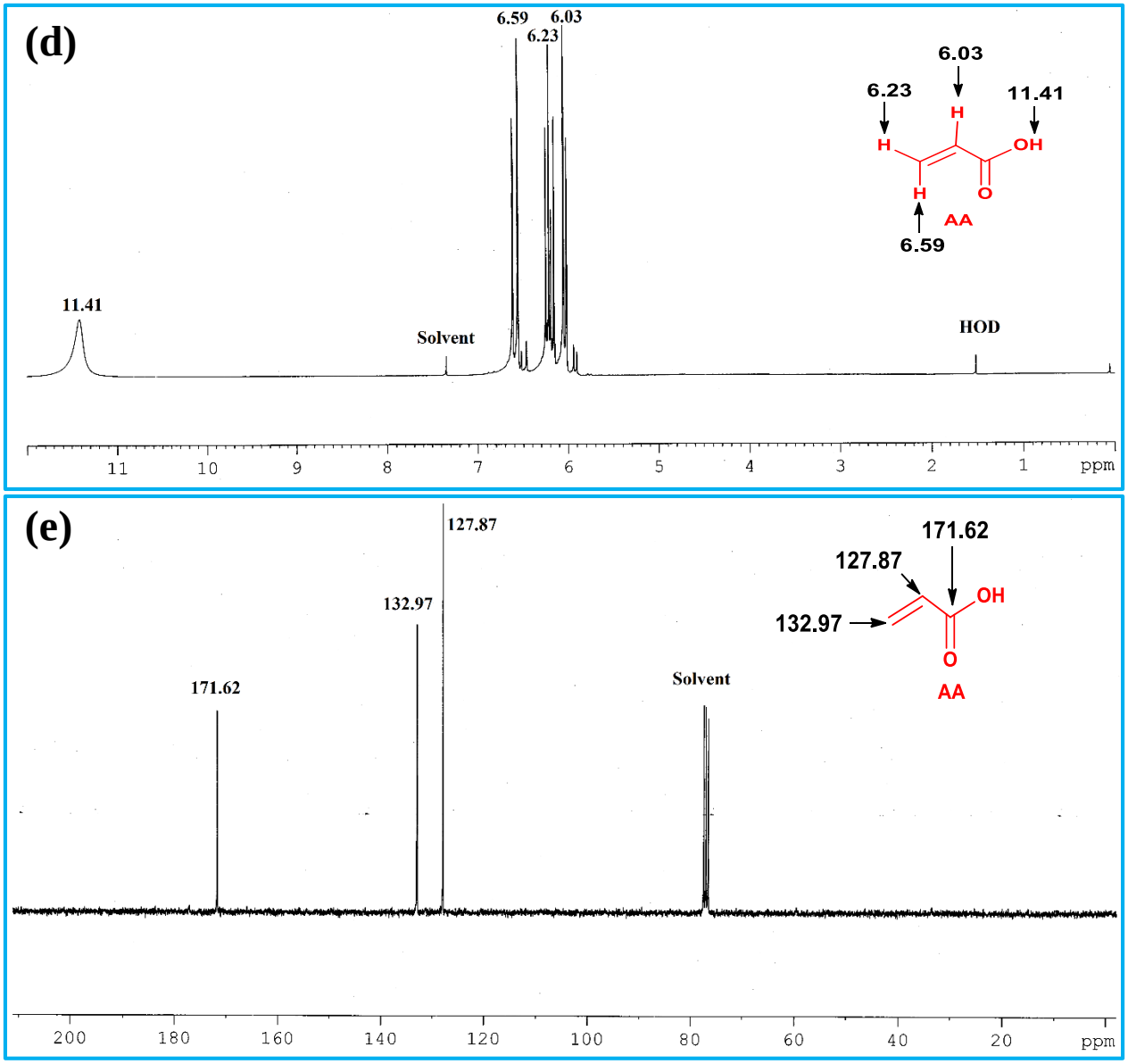
(d)
6.59
6.03
6.23
11.41
Solvent
HOD
6.03
6.23
11.41
H
H
OH
H
O
AA
6.59
11
10
9
8
7
6
5
4
3
2
1
ppm
(e)
127.87
132.97
171.62
Solvent
171.62
127.87
132.97
OH
O
AA
200
180
160
140
120
100
80
60
40
20
ppm

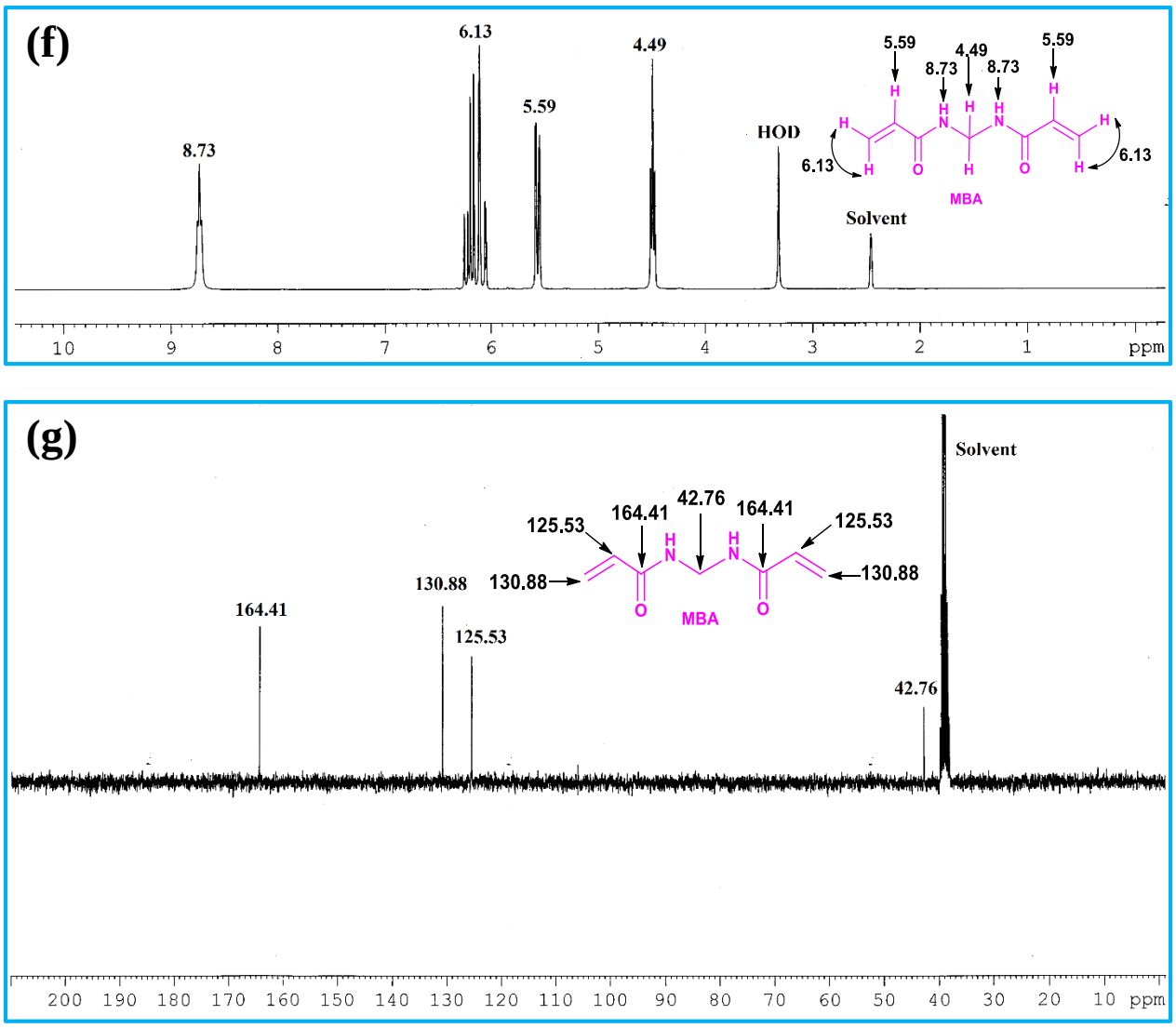

Figure S4. ^{1}H-NMR of (a) PN, (b) NIPAm, (d) AA and (f) MBA and ^{13}C-NMR of (c) NIPAm, (e) AA and (g) MBA

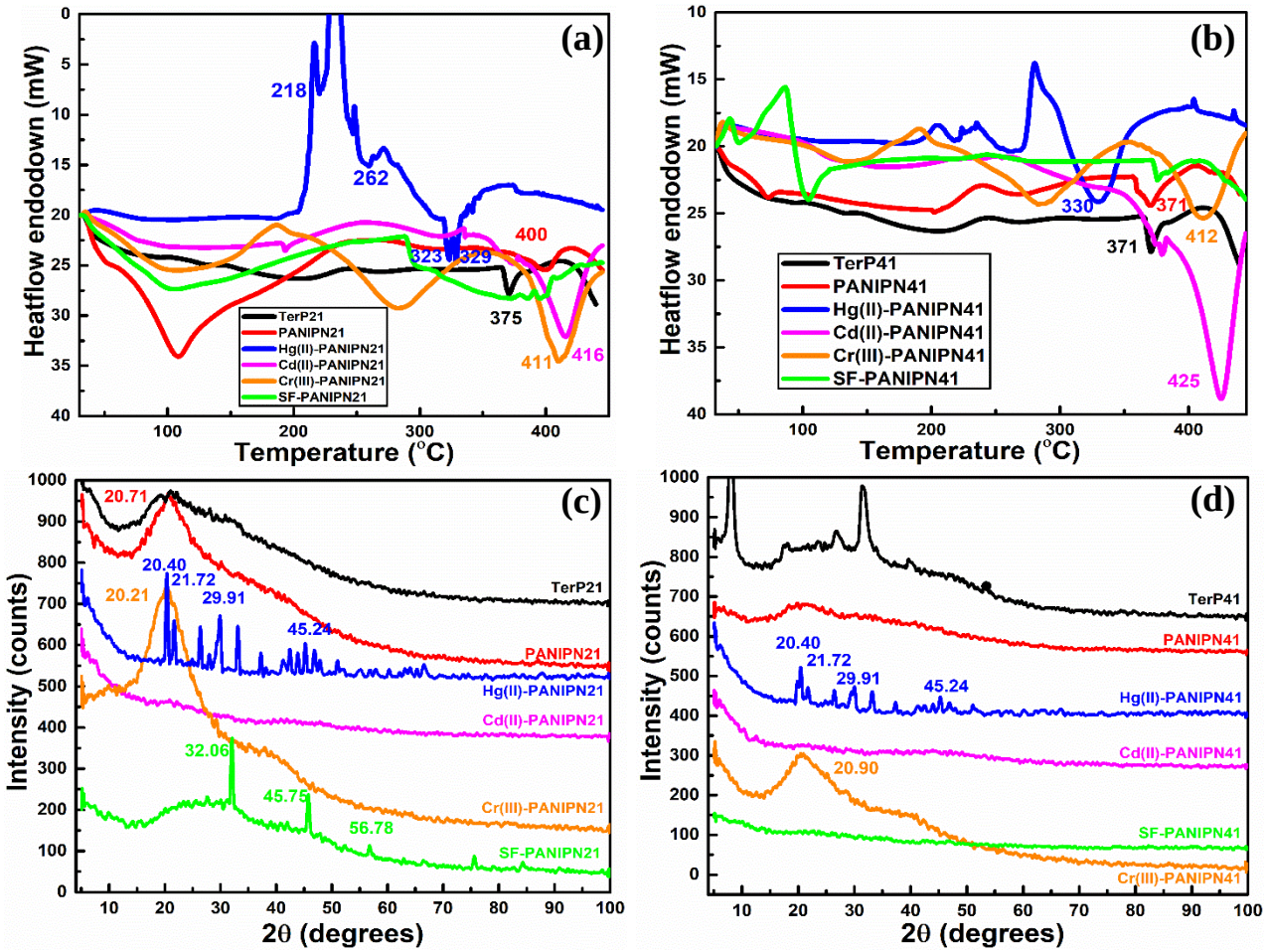

Figure S5. DSC of (a) TerP21, PANIPN21 and SF-, Hg(II)-, Cd(II)- and Cr(III)-PANIPN21, (b) TerP41, PANIPN41 and SF-, Hg(II)-, Cd(II)- and Cr(III)-PANIPN41; XRD of (c) TerP21, PANIPN21 and SF-, Hg(II)-, Cd(II)- and Cr(III)-PANIPN21, (d) TerP41, PANIPN41 and SF-, Hg(II)-, Cd(II)- and Cr(III)-PANIPN41

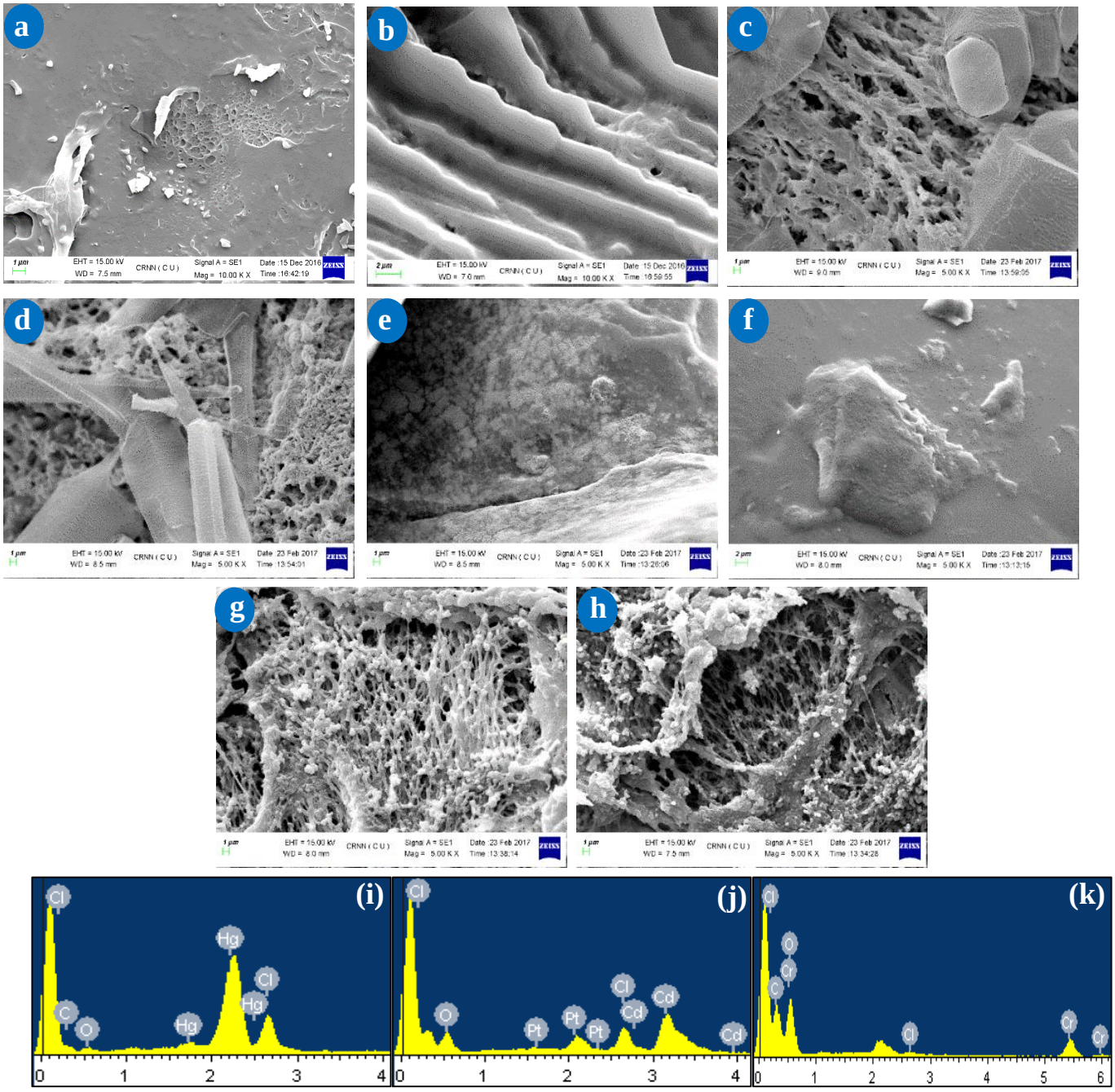

Figure S6. SEM photomicrographs of (a) PANIPN41, (b) PANIPN21, (c) Hg(II)-PANIPN41, (d) Hg(II)-PANIPN21, (e) Cd(II)-PANIPN41, (f) Cd(II)-PANIPN21, (g) Cr(III)-PANIPN41 and (h) Cr(III)-PANIPN21; EDX spectra of (i) Hg(II)-PANIPN21, (j) Cd(II)-PANIPN41 and (k) Cr(III)-PANIPN41

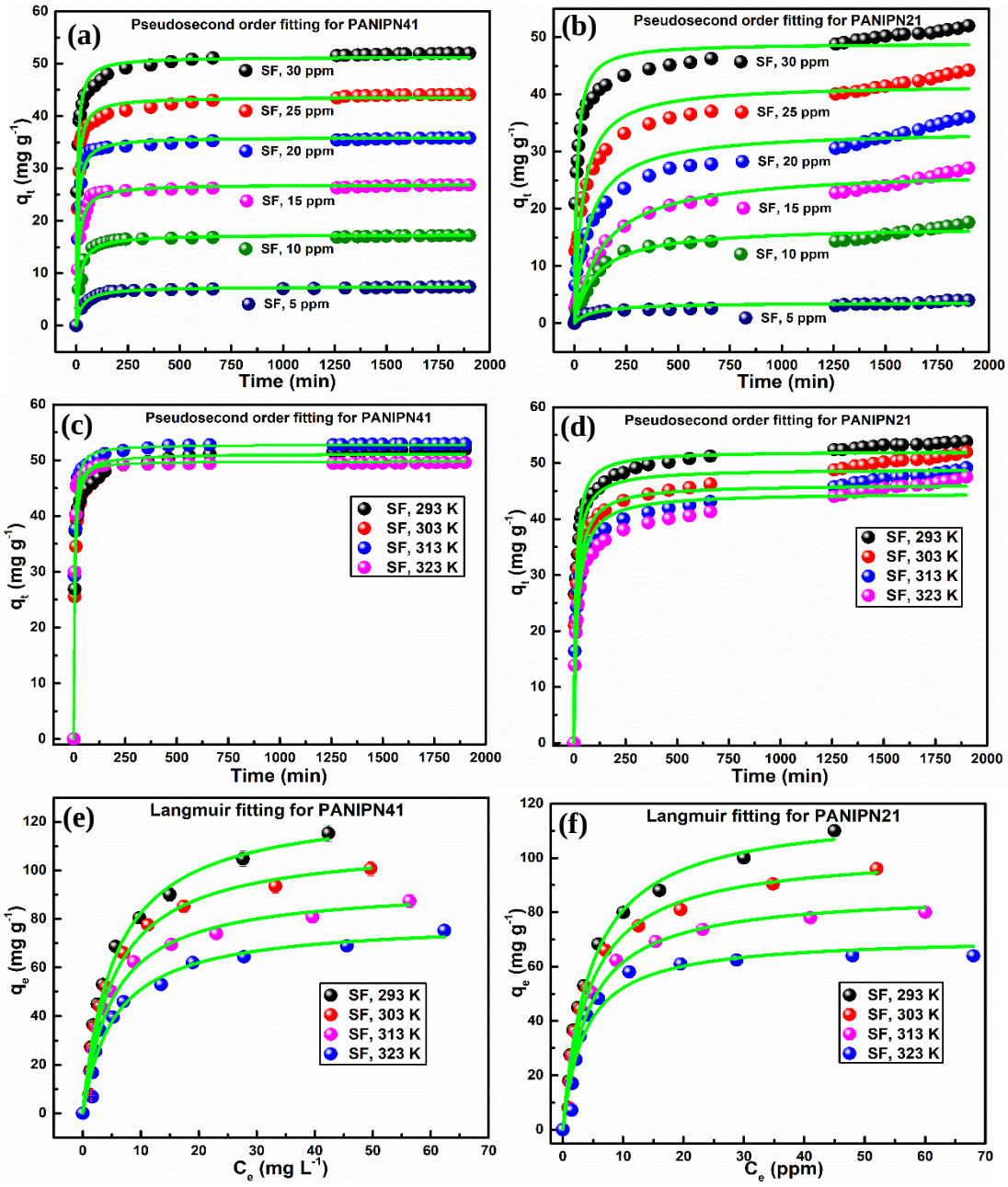

Figure S7. Pseudosecond order kinetics plots for (a) SF-PANIPN41 and (b) SF-PANIPN21 (pH_i = 9, T = 303 K and adsorbent dose = 0.5 g L^{-1}), pseudosecond order kinetics plots for (c) SF-PANIPN41 and (d) SF-PANIPN21 (pH_i = 9, C_o = 30 ppm and adsorbent dose = 0.5 g L^{-1}), nonlinear Langmuir isotherms fitting for (e) SF-PANIPN41 and (f) SF-PANIPN21

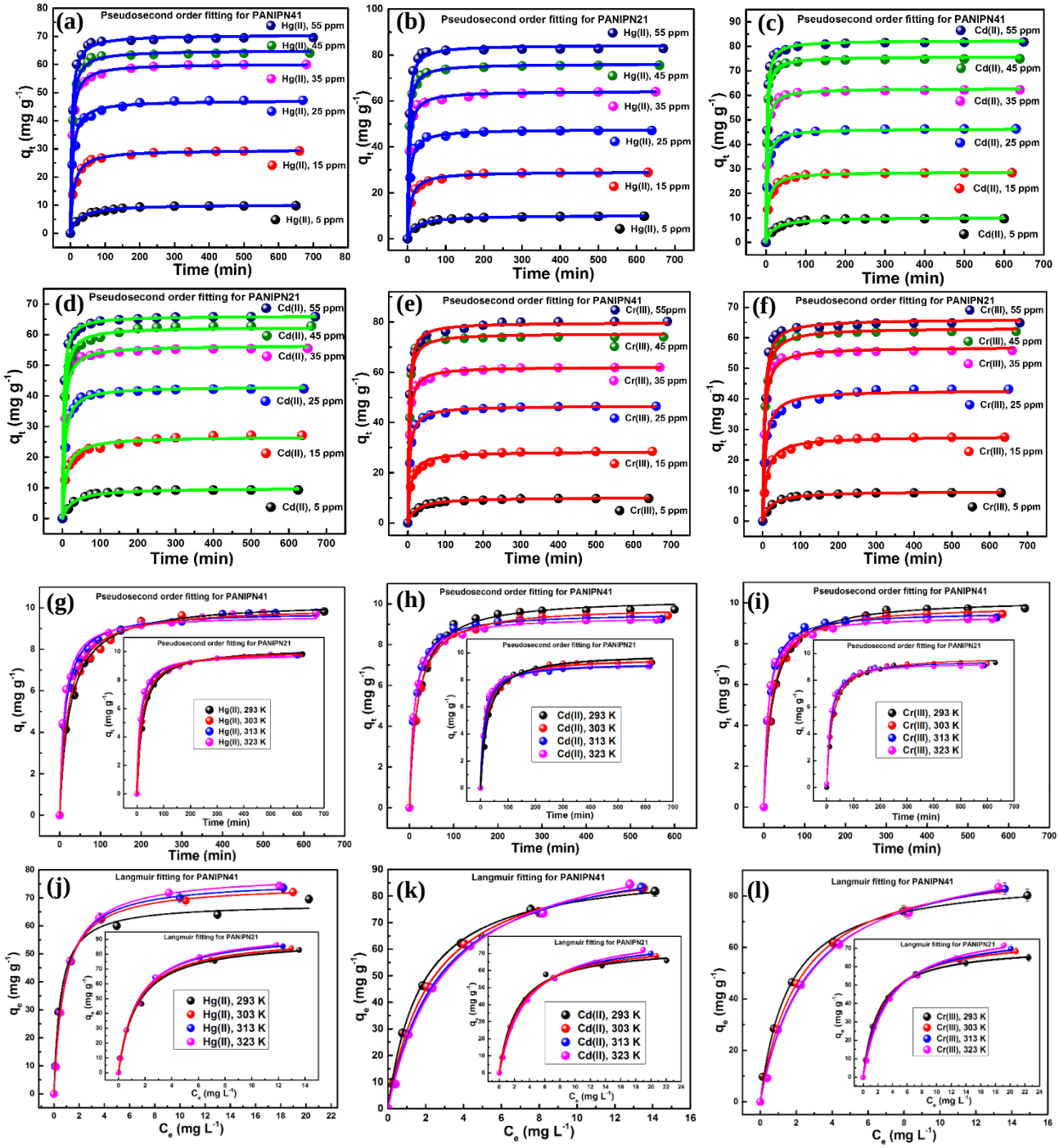

Figure S8. Pseudosecond order kinetics plots for (a) Hg(II)-PANIPN41, (b) Hg(II)-PANIPN21, (c) Cd(II)-PANIPN41, (d) Cd(II)-PANIPN21, (e) Cr(III)-PANIPN41 and (f) Cr(III)-PANIPN21 (pH_i = 7, T = 303 K and adsorbent dose = 0.5 g L^{-1}), pseudosecond order kinetics plots for (g) Hg(II)-PANIPN41, (h) Cd(II)-PANIPN41 and (i) Cr(III)-PANIPN41 and inset of (g), (h) and (i) show kinetics fitting for Hg(II)-PANIPN21, Cd(II)-PANIPN21 and Cr(III)-PANIPN21, respectively (pH_i = 7, C_o = 30 ppm and adsorbent dose = 0.5 g L^{-1}) and nonlinear isotherms fitting for (j) Hg(II)-PANIPN41, (k) Cd(II)-PANIPN41, (l) Cr(III)-PANIPN41 and inset of (j), (k) and (l) show isotherm fitting for Hg(II)-PANIPN21, Cd(II)-PANIPN21, and Cr(III)-PANIPN21, respectively

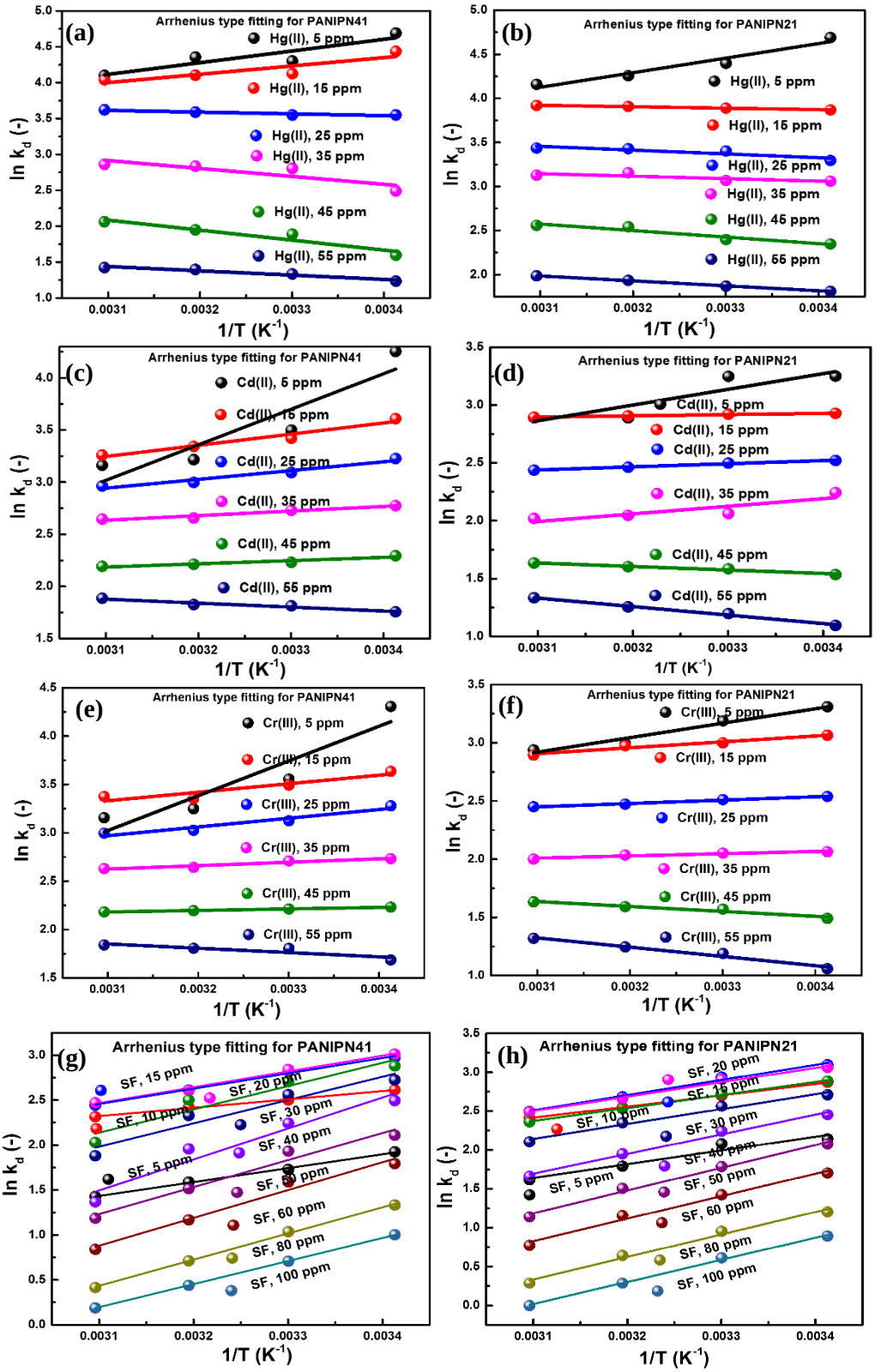

Figure S9. Plot of ln k_d vs. 1/T for (a) Hg(II)-PANIPN41, (b) Hg(II)-PANIPN21, (c) Cd(II)-PANIPN41, (d) Cd(II)-PANIPN21, (e) Cr(III)-PANIPN41, (f) Cr(III)-PANIPN21, (g) SF-PANIPN41, and (h) SF-PANIPN21 (pH_i = 7, T = 303 K, and adsorbent dose = 0.5 g L^{-1})

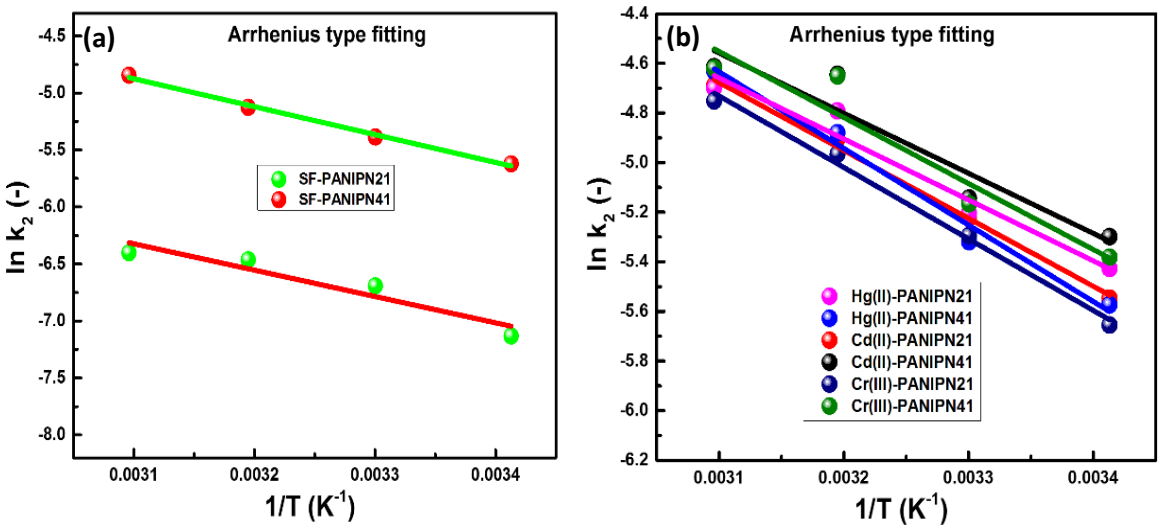

Figure S10. Plots of ln k_2 vs. 1/T for (a) SF-PANIPN21/41 and (b) Hg(II)-, Cd(II)- and Cr(III)-PANIPN21/41

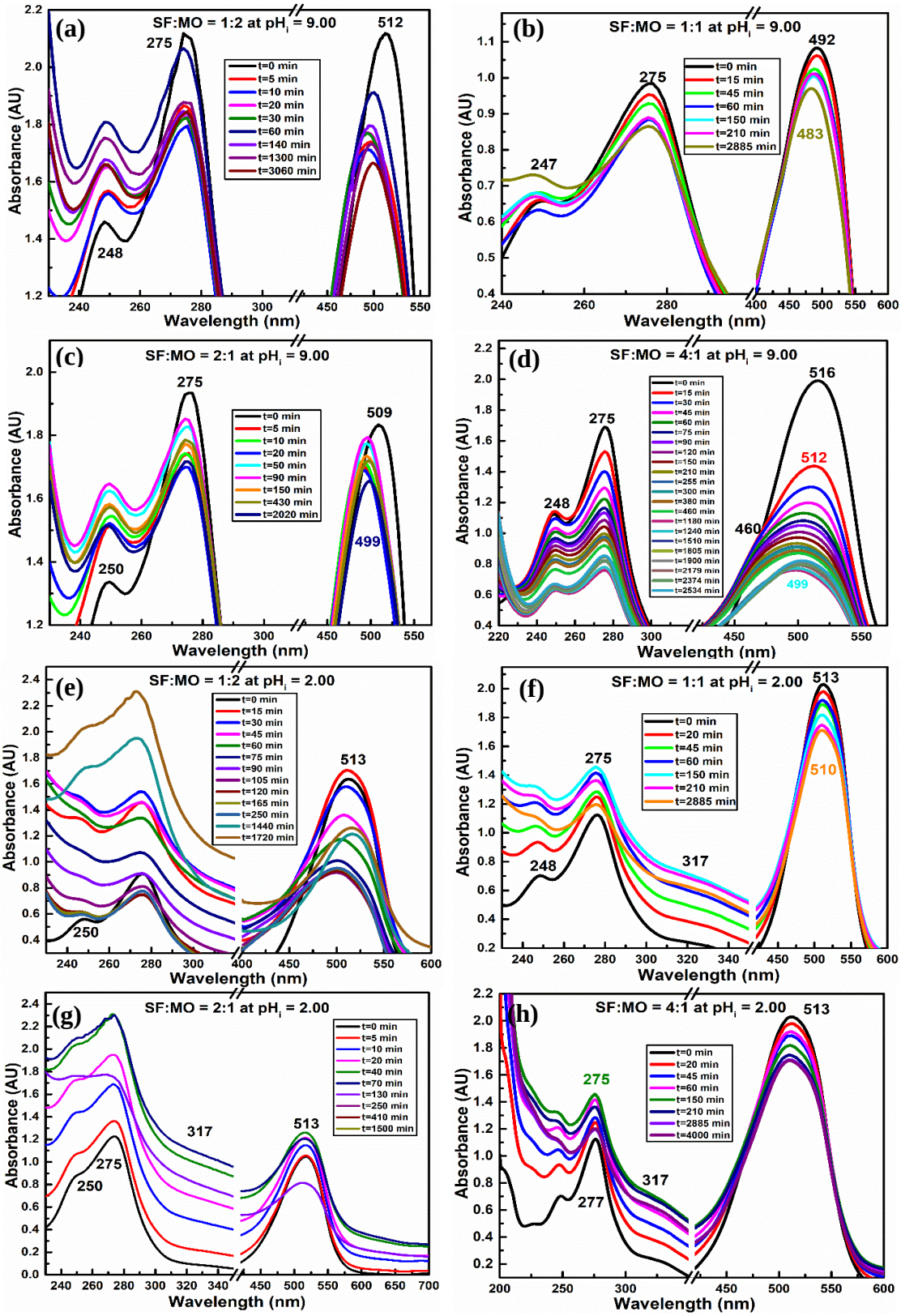

Figure S11. Synergistic removal of (a),(b),(c) and (d) SF-MO/pH$_i$ = 9/PANIPN21, (e),(f),(g) and (h) SF-MO/pH$_i$ = 2/PANIPN21 (C_o = 30 ppm, T = 303 K and adsorbent dose = 1 g L^{-1})

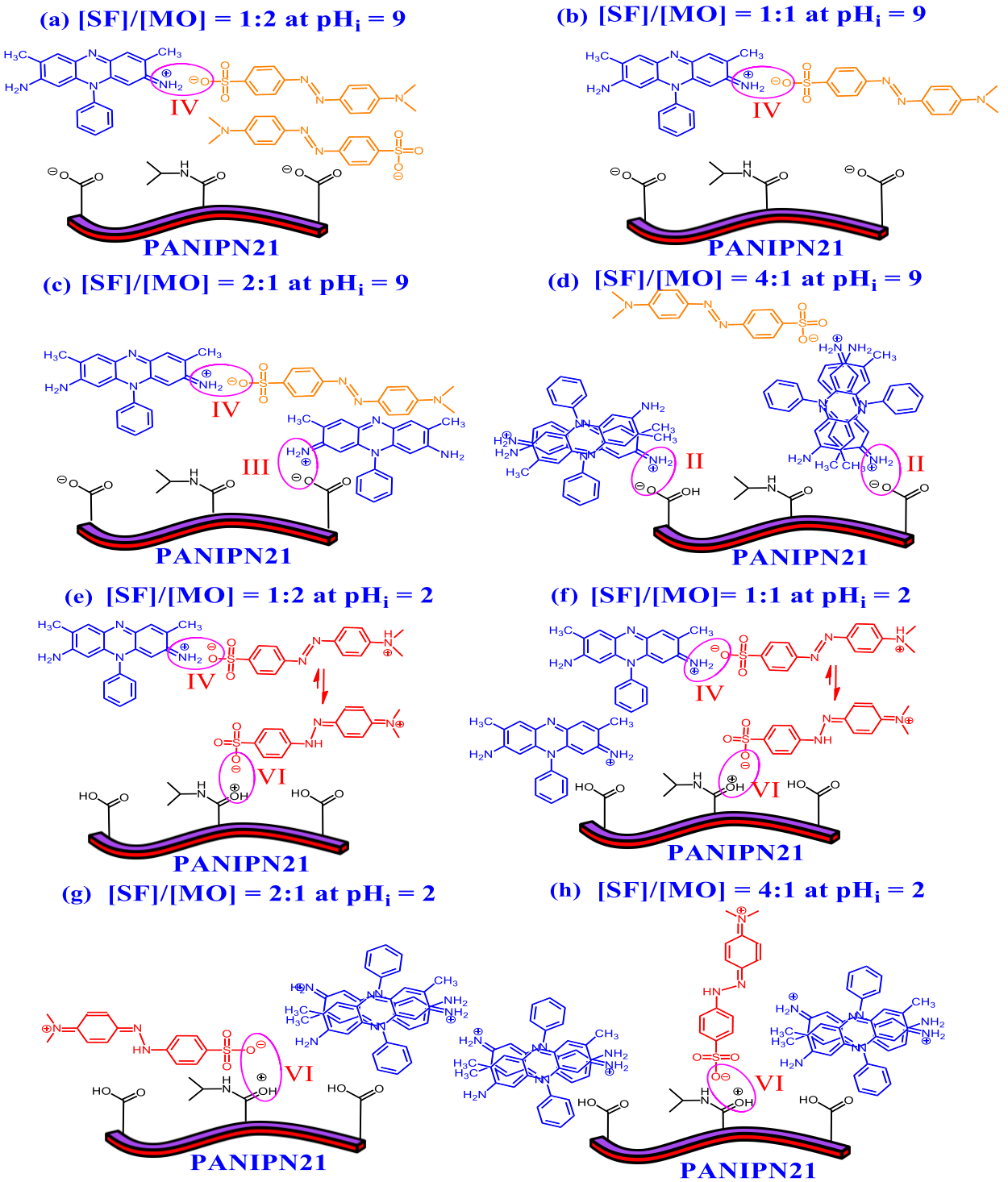

Scheme S1. Possible structure of MO-SF-PANIPN21 adduct (a-h) at pH_i = 9/2 involving ionic interaction between I. SF dimer and MO, II. SF dimer and PANIPN21, III. SF and PANIPN21, IV. SF and MO, V. MO and SA moiety of PANIPN21 and VI. MO and NIPAm moiety of PANIPN21

REFERENCES

(S1) Singha, N. R.; Karmakar, M.; Mahapatra, M.; Mondal, H.; Dutta, A.; Roy, C.; Chattopadhyay, P. K. Systematic synthesis of pectin-*g*-(sodium acrylate-*co*-N-isopropylacrylamide) interpenetrating polymer network for superadsorption of dyes/M(II): Determination of physicochemical changes in loaded hydrogels. *Polym. Chem*. **2017**, *8*, 3211–3237.

(S2) Zotov, N.; Keppler, H. The influence of water on the structure of hydrous sodium tetrasilicate glasses. *Am. Mineral*. **1998**, *83*, 823–834.

(S3) Hirashima, Y.; Sato, H.; Suzuki, A. ATR-FTIR spectroscopic study on hydrogen bonding of poly(N-isopropylacrylamide-*co*-sodium acrylate) gel. *Macromolecules* **2005**, *38*, 9280–9286.

(S4) Chen, J. J.; Ahmad, A. L.; Ooi, B. S. Poly(N-isopropylacrylamide-*co*-acrylic acid) hydrogels for copper ion adsorption: Equilibrium isotherms, kinetic and thermodynamic studies. *J. Environ. Chem. Eng*. **2013**, *1*, 339–348.

(S5) Socrates, G. Infrared and Raman characteristic group frequencies: Tables and charts. In The Carbonyl Group: C=O, 3rd ed.; John Wiley & Sons Ltd.: New York, 2001; pp 115–156.

(S6) Baum, A.; Dominiak, M.; Vidal-Melgosa, S.; Willats, W. G. T.; Søndergaard, K. M.; Hansen, P. W.; Meyer, A. S.; Mikkelsen, J. D. Prediction of pectin yield and quality by FTIR and carbohydrate microarray analysis. *Food Bioprocess Technol*. **2017**, *10*, 143–154.

(S7) Synytsya, A.; Novak, M. Structural analysis of glucans. *Ann. Transl. Med*. **2014**, *2*, 17–30.

(S8) Reis, A. V.; Guilherme, M. R.; Paulino, A. T.; Muniz, E. C.; Mattoso, L. H. C.; Tambourgi, E. B. Synthesis of hollow-structured nano- and microspheres from pectin in a nanodroplet emulsion. *Langmuir* **2009**, *25*, 2473–2478.

(S9) Thakur, S.; Pandey, S.; Arotiba, O. Development of a sodium alginate-based organic/inorganic superabsorbent composite hydrogel for adsorption of methylene blue. *Carbohyd. Polym*. **2016**, *153*, 34–46.

(S10) Zhao, S.; Li, J.; Wang, L.; Wang, X. Degradation of rhodamine B and safranin-T by MoO_3: CeO_2. *Clean–Soil Air Water* **2010**, *38*, 268–274.

(S11) Wei, W.; Hu, X.; Qi, X.; Yu, H.; Liu, Y.; Li, J.; Zhang, J.; Dong, W. A novel thermo-responsive hydrogel based on salecan and poly(N-isopropylacrylamide): Synthesis and characterization. *Colloid Surface B* **2015**, *125*, 1–11.

(S12) Shoulders, M. D.; Raines, R. T. Collagen structure and stability. *Annu. Rev. Biochem*. **2009**, *78*, 929–958.

(S13) Zhang, F.; Xiao, F.; Dong, Z. H.; Shi, W. Synthesis of polypyrrole wrapped graphene hydrogels composites as supercapacitor electrodes. *Electrochim. Acta* **2013**, *114*, 125–132.

(S14) Singha, N. R.; Kar, S.; Ray, S.; Ray, S. K. Separation of isopropyl alcohol-water mixtures by pervaporation using crosslink IPN membranes. *Chem. Eng. Process*. **2009**, *48*, 1020–1029.

(S15) El-Mohdy, H. L. A.; Hegazy, E. A.; El-Nesr, E. M.; El-Wah, M. A. Metal sorption behavior of poly(N-vinyl-2-pyrrolidone)/(acrylic acid-*co*-styrene) hydrogels synthesized by gamma radiation. *J. Environ. Chem. Eng*. **2013**, *1*, 328–338.

(S16) Cuggino, J. C.; Strumia, M. C.; Igarzabal, C. I. A. Synthesis, characterization and slow drug delivery of hydrogels based in N-acryloyl-tris-(hydroxymethyl) aminomethane and N-isopropyl acrylamide. *React. Funct. Polym*. **2011**, *71*, 440–446.

(S17) Spagnol, C.; Rodrigues, F. H. A.; Pereira, A. G. B.; Fajardo, A. R.; Rubira, A. F.; Muniz, E. C. Superabsorbent hydrogel composite made of cellulose nanofibrils and chitosan-graft-poly(acrylic acid). *Carbohyd. Polym*. **2012**, *87*, 2038–2045.

(S18) Irani, M.; Ismail, H.; Ahmad, Z. Preparation and properties of linear low-density polyethylene-g-poly (acrylic acid)/organo-montmorillonite superabsorbent hydrogel composites. *Polym. Test*. **2013**, *32*, 502–512.

(S19) Emara, A. A. A. Structural, spectral and biological studies of binuclear tetradentate metal complexes of N_3O Schiff base ligand synthesized from 4,6-Diacetylresorcinol and Diethylenetriamine. *Spectrochim. Acta A* **2010**, *77*, 117–125.

(S20) Tang, X.; Niu, D.; Bi, C.; Shen, B. Hg^{2+} adsorption from a low-concentration aqueous solution on chitosan beads modified by combining polyamination with Hg^{2+}-imprinted technologies. *Ind. Eng. Chem. Res*. **2013**, *52*, 13120–13127.

(S21) Wang, C.; Tao, S.; Wei, W.; Meng, C.; Liu, F.; Han, M. Multifunctional mesoporous material for detection, adsorption and removal of Hg^{2+} in aqueous solution. *J. Mater. Chem*. **2010**, *20*, 4635–4641.

(S22) Zhaoa, Y.; Chena, Y.; Li, M.; Zhou, S.; Xue, A.; Xing, W. Adsorption of Hg^{2+} from aqueous solution onto polyacrylamide/attapulgite. *J. Hazard. Mater*. **2009**, *171*, 640–646.

(S23) Hadavifar, M.; Bahramifar, N.; Younesi, H.; Li, Q. Adsorption of mercury ions from synthetic and real wastewater aqueous solution by functionalized multi-walled carbon nanotube with both amino and thiolated groups. *Chem. Eng. J.* **2014**, *237*, 217–228.

(S24) Zhang, C.; Sui, J.; Li, J.; Tang, Y.; Cai, W. Efficient removal of heavy metal ions by thiol-functionalized super paramagnetic carbon nanotubes. *Chem. Eng. J.* **2012**, *210*, 45–52.

(S25) Naushad, M.; ALOthman, Z. A.; Awual, M. R.; Alam, M. M.; Eldesoky, G. E. Adsorption kinetics, isotherms, and thermodynamic studies for the adsorption of Pb^{2+} and Hg^{2+} metal ions from aqueous medium using Ti(IV) iodovanadate cation exchanger. *Ionics* **2015**, *21*, 2237–2245.

(S26) Wang, Q.; Chang, X.; Li, D.; Hu, Z.; Li, R.; He, Q. Adsorption of chromium(III), mercury(II) and lead(II) ions onto 4-Aminoantipyrine immobilized nentonite. *J. Hazard. Mater.* **2011**, *186*, 1076–1081.

(S27) Dong, J.; Xu, Z.; Wang, F. Engineering and characterization of mesoporous silica-coated magnetic particles for mercury removal from industrial effluents. *Appl. Surf. Sci.* **2008**, *254*, 3522–3530.

(S28) Meena, A. K.; Kadirvelu, K.; Mishra, G. K.; Rajagopal, C.; Nagar, P. N. Adsorptive removal of heavy metals from aqueous solution by treated sawdust (*Acacia arabica*). *J. Hazard. Mater.* **2008**, *150*, 604–611.

(S29) Bai, L.; Hu, H. P.; Fu, W.; Wan, J.; Cheng, X.; Zhuge, L.; Xiong, L.; Chen, Q. Synthesis of a novel silica-supported Dithiocarbamate adsorbent and its properties for the removal of heavy metal ions. *J. Hazard. Mater.* **2011**, *195*, 261–275.

(S30) Say, R.; Birlik, E.; Denizli, A.; Ersöz, A. Removal of heavy metal ions by Dithiocarbamate-anchored polymer/organosmectite composites. *Appl. Clay Sci.* **2006**, *31*, 298–305.

(S31) Sui, Z.; Meng, Q.; Zhang, X.; Mab, R.; Cao, B. Green synthesis of carbon nanotube–graphene hybrid aerogels and their use as versatile agents for water purification. *J. Mater. Chem.* **2012**, *22*, 8767–8771.

(S32) Sreeprasad, T. S.; Maliyekkal, S. M.; Lisha, K. P.; Pradeep, T. Reduced graphene oxide-metal/metal oxide composites: Facile synthesis and application in water purification. *J. Hazard. Mater.* **2011**, *186*, 921–931.

(S33) Denizli, A.; Ozkan, G.; Arica, M. Y. Preparation and characterization of magnetic polymethylmethacrylate microbeads carrying Ethylene Diamine for removal of Cu(II), Cd(II), Pb(II), and Hg(II) from aqueous solutions. *J. App. Polym. Sci*. **2000**, *78*, 81–89.

(S34) Monier, M.; Abdel-Latif, D. A. Preparation of cross-linked magnetic chitosan-phenylthiourea resin for adsorption of Hg(II), Cd(II) and Zn(II) ions from aqueous solutions. *J. Hazard. Mater*. **2012**, *209–210*, 240–249.

(S35) Paulino, A. T.; Belfiore, L. A.; Kubota, L. T.; Muniz, E. C.; Almeida, V. C.; Tambourgi, E. B. Effect of magnetite on the adsorption behavior of Pb(II), Cd(II), and Cu(II) in chitosan-based hydrogels. *Desalination* **2011**, *275*, 187–196.

(S36) Dashtian, K.; Nasiri Azad, F.; Ghaedi, M.; Jamshidi, A.; Hassani, G.; Montazerozohori, M.; Hajati, S.; Rajabi, M.; Bazrafshan, A. A. Preparation and characterization of AC-Fe_3O_4-Au hybrid for simultaneous

removal of Cd^{2+}, Pb^{2+}, Cr^{3+} and Ni^{2+} ions from aqueous solution via complexation with 2-((2, 4-Dichloro-Benzylidene)-Amino)-Benzenethiol: Taguchi optimization. *RSC Adv*. **2016**, *6*, 19780–19791.

(S37) Yan, L.; Zhao, Q.; Jiang, T.; Liu, X.; Li, Y.; Fang, W.; Yin, H. Adsorption characteristics and behavior of a graphene oxide–Al_{13} composite for cadmium ion removal from aqueous solutions. *RSC Adv.* **2015**, *5*, 67372–67379.

(S38) Zhen, Z.; Wei, L. Effect of magnesium oxide on adsorption of Cd^{2+} from aqueous solution. *RSC Adv.* **2012**, *2*, 5178–5184.

(S39) Wang, X.; Liu, W.; Tian, J.; Zhao, Z.; Hao, P.; Kang, X.; Sang, Y.; Liu, H. Enhanced hydrogen desorption of an ammonia borane and lithium hydride system through synthesised intermediate compounds. *J. Mater. Chem. A* **2014**, *2*, 2599–2608.

(S40) Sulaymon, A. H.; Mohammed, A. A.; Al-Musawi, T. J. Comparative study of removal of cadmium (II) and chromium (III) ions from aqueous solution using low-cost biosorbent. *Int. J. Chem. Reac. Eng.* **2014**, *12*, 477–486.

(S41) Holan, Z. R.; Volesky, B.; Prasetyo, I. Biosorption of cadmium by biomass of marine algae. *Biotechnol. Bioeng.* **1993**, *41*, 819–825.

(S42) Xu, M.; Hadi, P.; Chen, G.; McKay, G. Removal of cadmium ions from wastewater using innovative electronic waste-derived material. *J. Hazard. Mater.* **2014**, *273*, 118–123.

(S43) Karthik, R.; Meenakshi, S. Removal of Pb(II) and Cd(II) ions from aqueous solution using polyaniline grafted chitosan. *Chem. Eng. J.* **2015**, *263*, 168–177.

(S44) Hlihor, R. M.; Diaconu, M.; Leon, F.; Curteanu, S.; Tavares, T.; Gavrilescu, M. Experimental analysis and mathematical prediction of Cd(II) removal by biosorption using support vector machines and genetic algorithms. *N. Biotechnol.* **2015**, *32*, 358–368.

(S45) Cheng, C.; Wang, J.; Yang, X.; Li, A.; Philippe, C. Adsorption of Ni (II) and Cd (II) from water by novel chelating sponge and the effect of alkali-earth metal ions on the adsorption. *J. Hazard. Mater.* **2014**, *264*, 332–341.

(S46) Ünlü, N.; Ersoz, M. Removal of heavy metal ions by using Dithiocarbamated sporopollenin. *Sep. Purif. Technol*. **2007**, *52*, 461–469.

(S47) Deng, J. H.; Zhang X. R.; Zeng, G. M.; Gong, J. L.; Niu, Q. Y.; Liang, J. Simultaneous removal of Cd(II) and ionic dyes from aqueous solution using magnetic graphene oxide nanocomposite as an adsorbent. *Chem. Eng. J.* **2013**, *226*, 189–200.

(S48) Bhunia, P.; Kim, G.; Baik, C.; Lee, H. A strategically designed porous iron–iron oxide matrix on graphene for heavy metal adsorption. *Chem. Commun.* **2012**, *48*, 9888–9890.

(S49) Deng, X.; Lü, L.; Li, H.; Luo, F. The adsorption properties of Pb(II) and Cd(II) on functionalized graphene prepared by electrolysis method. *J. Hazard. Mater.* **2010**, *183*, 923–930.

(S50) Lee, Y. C.; Yang, J. W. Self-assembled flower-like TiO_2 on exfoliated graphite oxide for heavy metal removal. *J. Ind. Eng. Chem.* **2012**, *18*, 1178–1185.

(S51) Zhao, G.; Li, J.; Ren, X.; Chen, C.; Wang, X. Few-layered graphene oxide nanosheets as superior sorbents for heavy metal ion pollution management. *Environ. Sci. Technol*. **2011**, *45*, 10454–10462.

(S52) Pour, Z. S.; Ghaemy, M. Removal of dyes and heavy metal ions from water by magnetic hydrogel beads based on poly(vinyl alcohol)/carboxymethyl starch-*g*-poly(vinyl imidazole). *RSC Adv.* **2015**, *5*, 64106–64118.

(S53) Ozay, O.; Ekici, S.; Baran, Y.; Kubilay, S.; Aktas, N.; Sahiner, N. Utilization of magnetic hydrogels in the separation of toxic metal ions from aqueous environments. *Desalination* **2010**, *260*, 57–64.

(S54) Pang, Y.; Zeng, G.; Tang, L.; Zhang, Y.; Liu, Y.; Lei, X.; Li, Z.; Zhang, J.; Xie, G. PEI-grafted magnetic porous powder for highly effective adsorption of heavy metal ions. *Desalination* **2011**, *281*, 278–284.

(S55) Li, J.; Jin, P.; Tang, C. Cr(III) adsorption by fluorinated activated boron nitride: A combined experimental and theoretical investigation. *RSC Adv.* **2014**, *4*, 14815–14821.

(S56) Guan, X.; Chang, J.; Chen, Y.; Fan, H. A magnetically-separable Fe_3O_4 nanoparticle surface grafted with polyacrylic acid for chromium(III) removal from tannery effluents. *RSC Adv.* **2015**, *5*, 50126–50136.

(S57) Yuan, X.; Wang, Y.; Wang, J.; Zhou, C.; Tang, Q.; Rao, X. Calcined graphene/MgAl-layered double hydroxides for enhanced Cr(VI) removal. *Chem. Eng. J.* **2013**, *221*, 204–213.

(S58) Ozay, O.; Ekici, S.; Baran, Y.; Aktas, N.; Sahiner, N. Removal of toxic metal ions with magnetic hydrogels. *Water Res.* **2009**, *43*, 4403–4411.

(S59) Tovar-Gómez, R.; Rivera-Ramírez, D. A.; Hernández-Montoya, V.; Bonilla-Petriciolet, A.; Durán-Valle, C. J.; Montes-Morán, M. A. Synergic adsorption in the simultaneous removal of acid blue 25 and heavy metals from water using a $Ca(PO_3)_2$-modified carbon. *J. Hazard. Mater.* **2012**, *199–200*, 290–300.

(S60) Mandal, B.; Ray, S. K. Removal of safranine T and brilliant cresyl blue dyes from water by carboxymethyl cellulose incorporated acrylic hydrogels: Isotherms, kinetics and thermodynamic study. *J. Taiwan Inst. Chem. E.* **2015**, *60*, 1–15.

(S61) Xu, X.; Bai, B.; Wang, H.; Suo, Y. Enhanced adsorptive removal of safranine T from aqueous solutions by waste sea buckthorn branch powder modified with dopamine: Kinetics, equilibrium, and thermodynamics. *J. Phys. Chem. Solids* **2015**, *87*, 23–31.

(S62) Roosta, M.; Ghaedi, M.; Daneshfar, A.; Sahraei, R. Experimental design based response surface methodology optimization of ultrasonic assisted adsorption of safaranin O by tin sulfide nanoparticle loaded on activated carbon. *Spectrochim. Acta A* **2014**, *122*, 223–231.

(S63) Ghaedi, M.; Haghdoust, S.; Nasiri Kokhdan, S.; Mihandoost, A.; Sahraie, R.; Daneshfar, A. Comparison of activated carbon, multiwalled carbon nanotubes, and cadmium hydroxide nanowire loaded on activated carbon as adsorbents for kinetic and equilibrium study of removal of safranine O. *Spectrosc. Lett.* **2012**, *45*, 500–510.

(S64) Zhao, X.; Wang, K.; Gao, Z.; Gao, H.; Xie, Z.; Du, X.; Huang, H. Reversing the dyes adsorption and separation performance of metal-organic frameworks via introduction of $–SO_3H$ groups. *Ind. Eng. Chem. Res.* **2017**, *56*, 4496–4501.

(S65) Nasiri Azad, F.; Ghaedi, M.; Dashtian, K.; Hajati, S.; Goudarzi, A.; Jamshidi, M. Enhanced simultaneous removal of malachite green and safranin O by ZnO nanorod-loaded activated carbon: Modeling, optimization and adsorption isotherms. *New J. Chem.* **2015**, *39*, 7998–8005.

(S66) Ghaedi, M.; Pakniat, M.; Mahmoudi, Z.; Hajati, S.; Sahraei, R.; Daneshfar, A. Synthesis of nickel sulfide nanoparticles loaded on activated carbon as a novel adsorbent for the competitive removal of methylene blue and safranin-O. *Spectrochim. Acta A* **2014**, *123*, 402–409.

(S67) Guler, U. A.; Ersan, M.; Tuncel, E.; Dügenci, F. Mono and simultaneous removal of crystal violet and safranin dyes from aqueous solutions by HDTMA-modified *Spirulina* sp. *Process Saf. Environ.* **2016**, *99*, 194–206.

(S68) Sahu, M. K.; Patel, R. K. Removal of safranin-O dye 1 from aqueous solution using modified red mud: Kinetic and equilibrium studies. *RSC Adv.* **2015**, *5*, 78491–78501.

(S69) Mohammed, M. A.; Ibrahim, A.; Shitu, A. Batch removal of hazardous safranin-O in wastewater using pineapple peels as an agricultural waste based adsorbent. *Int. J. Environ. Monit. Anal.* **2014**, *2*, 128–133.

(S70) Chowdhury, S.; Mishra, R.; Kushwaha, P.; Saha, P. Removal of safranin from aqueous solutions by NaOH-treated rice husk: Thermodynamics, kinetics and isosteric heat of adsorption. *Asia-Pac. J. Chem. Eng.* **2012**, *7*, 236–249.

(S71) Wahab, R.; Khan, F.; Kaushik, N. K.; Musarrat, J.; Al-Khedhairy, A. A. Photocatalytic TMO-NMs adsorbent: Temperature-time dependent safranine degradation, sorption study validated under optimized effective equilibrium models parameter with standardized statistical analysis. *Sci. Rep.* **2017**, *7*, 1–15.

(S72) Sahu, M. K.; Sahu, U. K.; Patel, R. K. Adsorption of safranin-O dye on CO_2 neutralized activated red mud waste: Process modelling, analysis and optimization using statistical design. *RSC Adv.* **2015**, *5*, 42294–42304.

(S73) Roosta, M.; Ghaedia, M.; Asfaram, A. Simultaneous ultrasonic-assisted removal of malachite green and safranin O by copper nanowires loaded on activated carbon: Central composite design optimization. *RSC Adv.* **2015**, *5*, 57021–57029.

(S74) Rotte, N. K.; Yerramala, S.; Boniface, J.; Srikanth, V. V. S. S. Equilibrium and kinetics of safranin O dye adsorption on MgO decked multi-layered graphene. *Chem. Eng. J.* **2014**, *258*, 412–419.